Focusing and Mode Separation of Elastic Vector Solitons in a 2D Soft Mechanical Metamaterial

Bolei Deng,[1] Chengyang Mo,[2] Vincent Tournat,[3,1] Katia Bertoldi,[1,4] and Jordan R. Raney[2,*]

[1]*Harvard John A. Paulson School of Engineering and Applied Sciences, Harvard University, Cambridge, Massachusetts 02138, USA*
[2]*Department of Mechanical Engineering and Applied Mechanics, University of Pennsylvania, Philadelphia, Pennsylvania 19104, USA*
[3]*Laboratoire d'Acoustique de l'Université du Mans, LAUM - UMR 6613 CNRS, Le Mans Université, France*
[4]*Kavli Institute, Harvard University, Cambridge, Massachusetts 02138, USA*

Soft mechanical metamaterials can support a rich set of dynamic responses, which, to date, have received relatively little attention. Here, we report experimental, numerical, and analytical results describing the behavior of an anisotropic two-dimensional flexible mechanical metamaterial when subjected to impact loading. We not only observe the propagation of elastic vector solitons with three components—two translational and one rotational—that are coupled together, but also very rich direction-dependent behaviors such as the formation of sound bullets and the separation of pulses into different solitary modes.

Ongoing advances in digital manufacturing technologies are enabling fabrication of systems with an unprecedented level of compositional and structural complexity [1–3]. This remarkable control of geometry has stimulated major advances in the design of mechanical metamaterials—designer matter with unique mechanical properties that are dictated by their engineered structure [4,5]. While initial efforts in the field have focused on systems with unusual linear properties, such as negative Poisson's ratio [6–8], negative stiffness [9,10], and negative thermal expansion [11,12], large deformation and nonlinearities have been recently embraced as a means toward new functionalities, including programmability [13], energy absorption [14], and shape transformation [15]. Moreover, it has been shown that highly deformable mechanical metamaterials can be designed to support the propagation of a variety of nonlinear waves with large displacement amplitudes [16–19], providing a convenient platform to study nonlinear wave physics. However, to date the investigation of the nonlinear dynamic response of flexible metamaterials has been limited to one-dimensional (1D) systems.

Here, we investigate the nonlinear dynamic response of a 2D flexible mechanical metamaterial comprising a periodic arrangement of squares connected at their vertices by thin ligaments [18,20,21]. Remarkably, our experiments and analyses reveal that several new physical phenomena emerge when subjecting the structure to low-energy impacts. First, our system supports the propagation of elastic vector solitons with three polarization components—two translational and one rotational. Second, we investigate the effect of the anisotropy of the medium on the 2D nature of the soliton and find that such anisotropy plays a crucial role, leading to rich new nonlinear effects. For example, for propagation at 45° from the symmetry axis, a distinct focusing effect is

observed. The pulse does not spread along either direction, suggesting that sound bullets may exist in our system. Moreover, we find that for most other propagation angles the wave separates into two distinct solitary modes, each following a principal direction of symmetry. While 2D nonlinear elastic waves have been previously studied in granular media [22–25], the monolithicity and printability of our system allow facile control of the architecture, and hence control of the system's nonlinear dynamic response, providing a powerful platform to explore, visualize, and engineer new wave phenomena.

We start by studying experimentally the response of a 2D circular sample with 30 squares along its diameter when excited with an impactor [see Fig. 1(a)]. Our sample is fabricated out of polydimethylsiloxane using direct ink writing, an extrusion-based 3D printing approach [26]. Steel spheres with a diameter of 4.35 mm are embedded in the middle of the squares to modify their inertial properties. All squares are rotated by offset angles of $\theta_0 = 25°$, have center-to-center-distance of $a = 9.27$ mm, and are connected to one another by ligaments approximately 5 mm in width [see Fig. 1(b)]. In our experiments, we impact the sample at different points along its circumference to initiate pulses that propagate along different directions defined as

$$\hat{\mathbf{e}}_{\parallel} = \cos\phi\hat{\mathbf{e}}_x + \sin\phi\hat{\mathbf{e}}_y, \qquad (1)$$

where $\hat{\mathbf{e}}_x$ and $\hat{\mathbf{e}}_y$ denote the two directions of periodicity of the system, and impact angle ϕ is the angle between the normal to the impactor and $\hat{\mathbf{e}}_x$ [see Fig. 1(a)]. Finally, we record the impact event with a high speed camera, allowing measure of local vectorial displacement and velocity via digital image correlation [27,28] (see the Supplemental Material [29] for additional information).
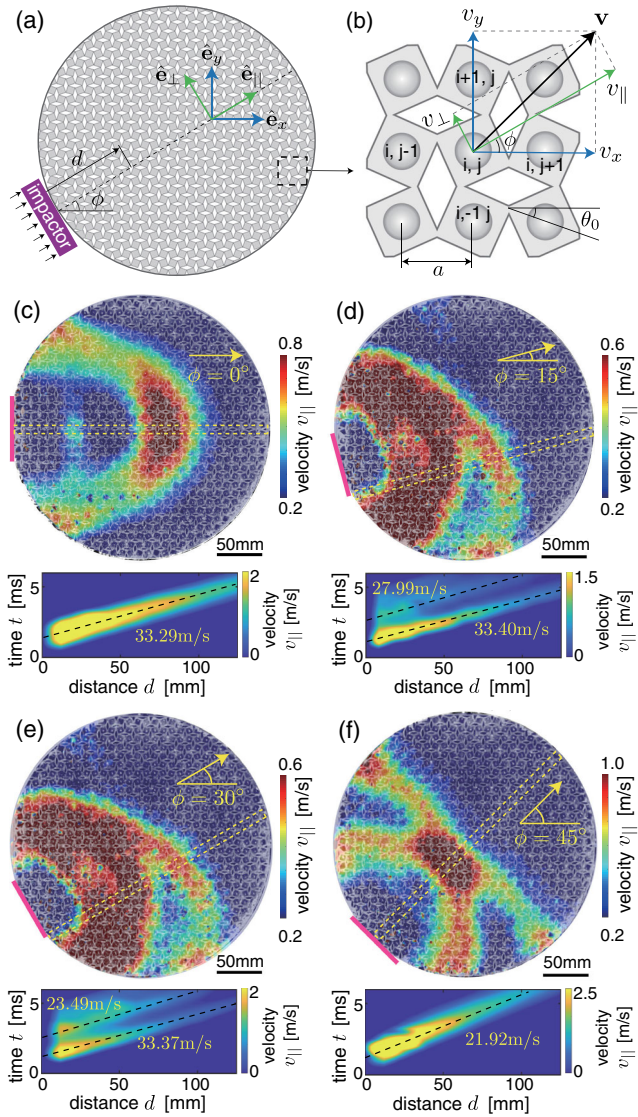
FIG. 1. (a) Schematic of the system. (b) Definition of velocity of squares. (c)–(f) Contour plots of parallel velocity $v_\parallel$ and t-d contour plots of velocity along indicated direction for impact angles of $\phi = 0°$, 15°, 30°, and 45°. The magenta squares are those to which the displacement is applied. The full time evolution is available in Movie S1 of the Supplemental Material [29].

In Figs. 1(c)–1(f), we report contour plots of the velocity along $\hat{\mathbf{e}}_\parallel$, $v_\parallel$, at $t = 5.5$ ms after impact for $\phi = 0°$, 15°, 30°, and 45°. Moreover, for each impact angle we also show the spatial-temporal evolution of $v_\parallel$ along the propagation direction (focusing on the region delimited by the yellow dashed lines in the snapshots), allowing extraction of pulse speed (details in the Supplemental Material [29]). Three key features emerge from these plots. First, for impact angle $\phi = 0°$ the pulse propagates in a solitary fashion (i.e., it maintains both its shape and velocity), as the velocity profile is characterized by a single peak with nearly constant width. Second, for $\phi = 15°$ and 30° the excitation

splits into two separate pulses. This is apparent both from the asymmetric velocity profile and from the two peaks seen in the spatial-temporal evolution of $v_\parallel$, each with constant velocity and pulse width. Third, for $\phi = 45°$ we again have a single pulse propagating through the sample, but this time the wave front keeps its shape in both the $\mathbf{e}_\parallel$ and $\mathbf{e}_\perp$ directions. As a matter of fact, the pulse transversal width is the same as the impactor width (see the Supplemental Material [29] for more details). This suggests that for $\phi = 45°$ the wave has a transversal self-focusing effect, balancing the linear beam diffraction and stabilizing the pulse lateral width. This potentially leads to the generation of compact sound bullets of very large amplitudes, which may dramatically impact a variety of applications, such as biomedical devices, nondestructive evaluation, and defense systems [30–32].

To better understand our experimental results, we numerically model the system as an array of rigid squares connected at their vertices via a combination of linear axial (with stiffness $k_s = 8180$ N/m and $k_l = 16360$ N/m) and rotational springs (with stiffness $k_\theta = 0.0312$ N m/rad) [18,33,34]. Moreover, we assign to the $[i, j]$th square three degrees of freedom (DoF): the displacement in the $\hat{\mathbf{e}}_x$ direction, $u_x^{[i,j]}$, the displacement in the $\hat{\mathbf{e}}_y$ direction, $u_y^{[i,j]}$, and the rotation around the z axis, $\theta^{[i,j]}$. Using these definitions, the equations of motion for the $[i, j]$th square are given by

$$m\ddot{u}_\gamma^{[i,j]} = \sum_{p=1}^{4} F_p^{\gamma[i,j]}, \qquad J\ddot{\theta}^{[i,j]} = \sum_{p=1}^{4} M_p^{[i,j]}, \qquad (2)$$

where $\gamma = x$, y, and $m = 0.797$ g and $J = 5.457$ g mm^2 are, respectively, the mass and moment of inertia of the rigid units. Moreover, $F_p^{x[i,j]}$ and $F_p^{y[i,j]}$ are the forces along the $\hat{\mathbf{e}}_x$ and $\hat{\mathbf{e}}_y$ directions generated at the pth vertex of the $[i, j]$th unit by the springs, and $M_p^{[i,j]}$ represents the corresponding moment (see the Supplemental Material [29] for their explicit expressions).

By numerically solving Eq. (2) via the fourth order Runge-Kutta method, we find that the physical phenomena observed in our tests (i.e., solitonlike pulses, mode separation for $\phi = 15°$ and 30°, and self-focusing for $\phi = 45°$) not only persist, but actually become more accentuated when considering a larger model with 60 squares along the diameter (see Fig. 2 and the Supplemental Material [29]). Furthermore, in our numerical analysis we also excite planar waves on square-shaped samples and again observe solitonlike pulses and separation of modes (see Fig. S11 of the Supplemental Material [29]). As such, our numerical results indicate that the phenomena observed in the experiments are not artifacts introduced by either edge effects, damping or excitation, but rather emerge because of the bulk properties of the medium.
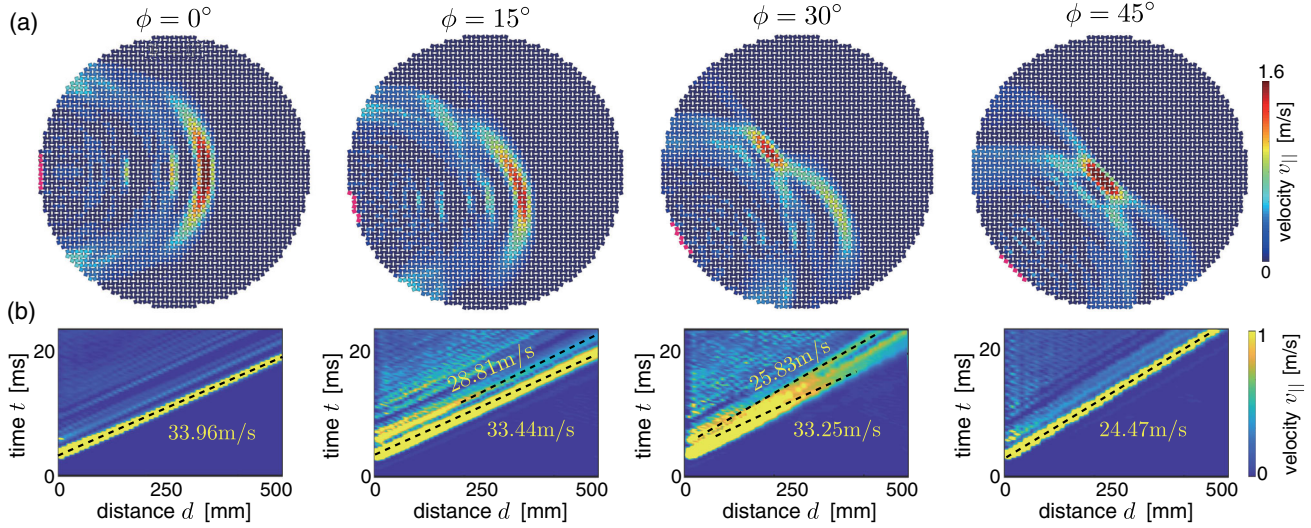
FIG. 2. Numerical results for a circular model with 60 squares along its diameter. (a) Contour plots of $v_\parallel$ at $t = 12$ ms for all four impact angles. (b) Spatial-temporal map of $v_\parallel$ for all considered impact angles. The magenta squares in (a) are those to which the displacement is applied. The full time evolution is available in Movie S2 of the Supplemental Material [29].
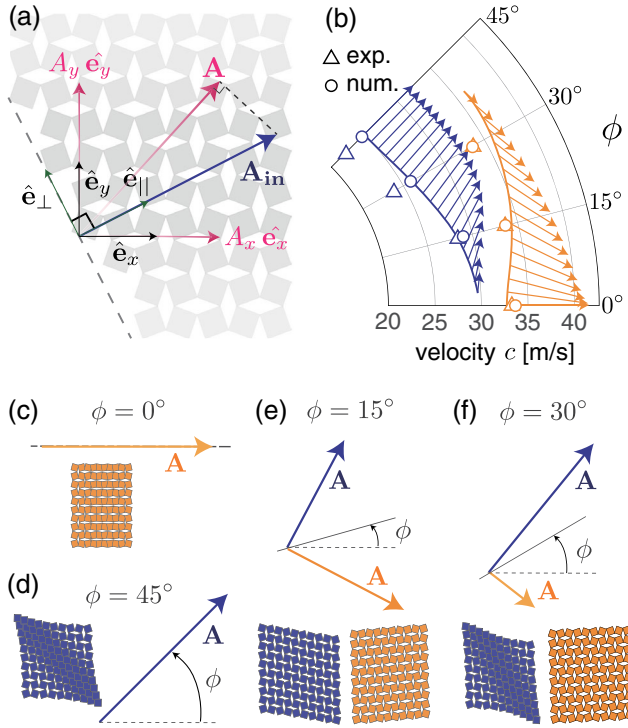

FIG. 3. (a) Schematic highlighting the input signal $\mathbf{A_{in}}$ and the translational amplitude of the excited soliton $\mathbf{A}$. (b) Translational amplitude $\mathbf{A}$ of the solitons excited by impacts of amplitude $A_{in} = 7$ mm for $\phi \in [0, 45°]$. The triangular and circular markers correspond to the velocities extracted from our experimental and numerical results. (c)–(f) Translational amplitude and associated deformation for all solitary modes. Note that the displacements and rotations are five times amplified, excited by input signals with $A_{in} = 7$ mm and (c) $\phi = 0°$, (d) $\phi = 45°$, (e) $\phi = 15°$, and (f) $\phi = 30°$.

Since our numerical results reveal that the phenomena observed in our experiments are a robust feature of the system, we next explore deeper insights into the nonlinear dynamic properties of our system by simplifying Eq. (2) to derive analytical solutions for the case of planar waves. To this end, we assume that the wavelength of the propagating waves is much wider than the cell size a and that $\theta^{[i,j]} \ll 1$. We then take the continuum limit of Eq. (2) and retain nonlinear terms up to the third order to obtain the continuum governing equations

$$m\ddot{u}_x = a^2 \left(k_l \partial_{xx} u_x + k_s \partial_{yy} u_x + \frac{\tan\theta_0 a^2 k_l}{6} \partial_{xxx}\theta \right.$$
$$\left. + k_l(\tan\theta_0 + \theta - \tan\theta_0\theta^2/2)\partial_x\theta \right), \quad (3a)$$

$$m\ddot{u}_y = a^2 \left[k_s \partial_{xx} u_y + k_l \partial_{yy} u_y + \frac{\tan\theta_0 a^2 k_l}{6} \partial_{yyy}\theta \right.$$
$$\left. + k_l(\tan\theta_0 + \theta - \tan\theta_0\theta^2/2)\partial_y\theta \right], \quad (3b)$$

$$J\ddot{\theta} = a^2(k_s - k_l\tan^2\theta_0 - 4k_\theta)\nabla^2\theta/4$$
$$- 2a^2(k_l\tan^2\theta_0 + 4k_\theta)\theta - 3a^2k_l\tan\theta_0\theta^2$$
$$- a^2k_l(\tan\theta_0 + \theta - \tan\theta_0\theta^2/2)(\partial_x u_x + \partial_x u_y)$$
$$- a^2k_l(13 - 15\tan^2\theta_0)\theta^3/12, \quad (3c)$$

where $\partial_\gamma f = \partial f/\partial\gamma$, $\nabla^2 = \partial_{xx} + \partial_{yy}$, and u_x, u_y, and θ are three continuous functions which interpolate the discrete

variables $u_x^{[i,j]}$, $u_y^{[i,j]}$, and $\theta^{[i,j]}$, respectively (see the Supplemental Material [29] for details).

To solve Eq. (3), we focus on planar waves propagating along the $\hat{\mathbf{e}}_\parallel$ direction and introduce the traveling coordinate $\zeta = x \cos \phi + y \sin \phi - ct$, with c being the pulse velocity. Introduction of ζ into Eq. (3), integration of Eqs. (3a) and (3b) with respect to ζ and their subsequent substitution into Eq. (3c), yields

$$d_{\zeta\zeta}\theta = C_1\theta + C_2\theta^2 + C_3\theta^3, \qquad (4)$$

with

$$\begin{aligned}
C_1 &= -4F[(E_1^x + E_1^y - 2)\sin^2\theta_0 - 2K_\theta], \\
C_2 &= -3F \sin 2\theta_0 (E_1^x + E_1^y - 2), \\
C_3 &= -F(7\cos 2\theta_0 - 1)(E_1^x + E_1^y - 2)/3, \qquad (5)
\end{aligned}$$

and

$$\begin{aligned}
E_\gamma^x &= \frac{\cos^{2\alpha}\phi}{\cos^2\phi + \frac{k_s}{k_l}\sin^2\phi - \frac{mc^2}{k_l a^2}}, \\
E_\gamma^y &= \frac{\sin^{2\alpha}\phi}{\frac{k_s}{k_l}\cos^2\phi + \sin^2\phi - \frac{mc^2}{k_l a^2}}, \\
F &= \frac{3k_l\sec^2\theta_0/2}{a^2[\frac{3k_s}{2} + k_l\tan^2\theta_0(E_2^x + E_2^y - \frac{3}{2})] - 6(k_\theta - \frac{k_l c^2 J}{ma^2})}, \qquad (6)
\end{aligned}$$

where $\gamma = 1, 2$. Equation (4) can be directly derived from the Klein-Gordon equation with quadratic and cubic nonlinearities [35,36], by substitution of the traveling wave coordinate ζ. It admits well-known solitary wave solutions of the form

$$\theta = \frac{1}{D_1 \pm D_2 \cosh(\zeta/W)}, \qquad (7)$$

where

$$D_1 = -\frac{C_2}{3C_1}, \quad D_2 = \sqrt{\frac{C_2^2}{9C_1^2} - \frac{C_3}{2C_1}}, \quad \text{and} \quad W = \frac{1}{\sqrt{C_1}}. \qquad (8)$$

Finally, the solution for the translational components u_x and u_y can be obtained by integrating Eqs. (3a) and (3b) with respect to ζ (see the Supplemental Material [29] for details).

Having obtained an analytical solitary wave solution, we now use it to validate our experimental and numerical observations. To begin with, we note that the analytical solution confirms that the pulses propagating in our 2D mechanical metamaterial are solitons. Specifically, it reveals that they are elastic vector solitons with three components—two translational and one rotational—that are coupled together and copropagate without dispersion. Note that although the springs used here are all linear, the

nonlinearity still emerges from the "+1" rotational DoF through its nonlinear geometrical coupling between the two translational DoF. Next, we use our continuum model to understand whether for specific loading directions ϕ the system supports solitary waves with different modes. To this end, we start by noting that in our experiments the impactor imposes a displacement with amplitude

$$\mathbf{A}_{\text{in}} = A_{\text{in}}\hat{\mathbf{e}}_\parallel = A_{\text{in}}\cos\phi\,\hat{\mathbf{e}}_x + A_{\text{in}}\sin\phi\,\hat{\mathbf{e}}_y, \qquad (9)$$

to the squares that it contacts. This input signal excites a vector soliton with translational amplitude

$$\mathbf{A} = A_x\hat{\mathbf{e}}_x + A_y\hat{\mathbf{e}}_y, \qquad (10)$$

where A_x and A_y are the amplitudes of its translational components, which are functions of both the propagation velocity c and the propagation angle ϕ [i.e., $A_x(c, \phi)$ and $A_y(c, \phi)$] (see the Supplemental Material [29] for details). Since the translational amplitude should be a projection of the input signal along the direction of $\mathbf{A}$ [see Fig. 3(a)], it follows that

$$|\mathbf{A}| = \sqrt{A_x^2 + A_y^2} = \mathbf{A}_{\text{in}} \cdot \frac{\mathbf{A}}{|\mathbf{A}|}, \qquad (11)$$

which provides a relation between the input signal applied by the impactor (i.e., the amplitude A_{in} and the angle ϕ) and the propagating velocity c of the excited solitary wave. Therefore, given a pair of input parameters ϕ and A_{in}, Eq. (11) can be used to solve for c and, once c is known, the form of the solitary pulse excited by the impact via Eqs. (7), (3a), and (3b).

In Fig. 3(b), we show the evolution as a function of the angle ϕ of $\mathbf{A}$ and c for solitons excited by impacts of amplitude $A_{\text{in}} = 7$ mm (the input displacement applied in our experiments). Interestingly, we find that for most impact directions two different solitary modes are excited by $\mathbf{A}_{\text{in}}$, each characterized by a distinct velocity c and translational amplitude $\mathbf{A}$. Only for impact directions of $\phi \sim 0°$ and $\sim 45°$ is a single wave mode excited. Importantly, we also find that the velocities predicted by our continuum model nicely agree with those extracted from both our experimental (triangular markers) and numerical (circular markers) results. Finally, to get a better understanding of the different solitary modes excited by the input signal, in Figs. 3(c)–3(f) we show a snapshot of the deformation induced by all excited modes for $\phi = 0°$, $15°$, $30°$, and $45°$. We find that, while for $\phi = 0°$ and $45°$ a pure compression wave propagates through the structure (i.e., all squares moves along the $\hat{\mathbf{e}}_\parallel$ direction), for $\phi = 15°$ and $\phi = 30°$ two mixed compression-shear solitary modes are excited—a prediction that matches well with our experimental and numerical results.

Finally, we focus on the transversal self-focusing effect observed both in our experiments and numerical analyses
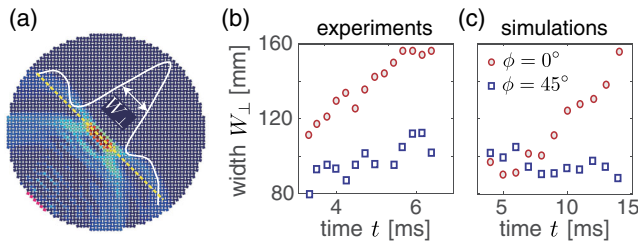
FIG. 4. (a) Schematic highlighting the full width at half maximum, $W_\perp$. (b),(c) Time evolution of $W_\perp$ as extracted from (b) experiments and (c) simulations for $\phi = 0°$ (red markers) and $\phi = 45°$ (blue markers).

for $\phi = 45°$. To better quantify it, for $\phi = 0°$ and $45°$ we extract from both our experiments and numerical simulations the width of the propagating pulses along the $\hat{\mathbf{e}}_\perp$ direction, $W_\perp$ (see the Supplemental Material [29] for details). The results shown in Figs. 4(b) and 4(c) indicate that $W_\perp$ is rather constant with time (or equivalently distance) for $\phi = 45°$ and that its variation is significantly smaller relative to that observed for $\phi = 0°$. As such, this analysis confirms the self-focusing effect observed in the contour plots of Figs. 1 and 2 for $\phi = 45°$.

To summarize, we have used a combination of experimental, numerical, and analytical methods to study the propagation of nonlinear elastic waves in a 2D soft mechanical metamaterial comprising a network of squares connected by thin and highly deformable ligaments. Our results reveal that the system supports not only the propagation of elastic vector solitons with three components (two translational and one rotational), but also very rich behaviors such as compact pulses (akin to sound bullets) and separation of the pulses into different solitary modes. As such, our study shows that soft mechanical metamaterials provide a convenient platform to study nonlinear wave physics. Moreover, the 3D printability of these systems enables unique opportunities for engineering wave phenomena, ultimately providing new opportunities to control and manage intense vibrations and waves.

*Corresponding author.
raney@seas.upenn.edu

[1] J. R. Raney and J. A. Lewis, Printing mesoscale architectures, MRS Bull. 40, 943 (2015).

[2] T. A. Schaedler and W. B. Carter, Architected cellular materials, Annu. Rev. Mater. Res. 46, 187 (2016).

[3] R. L. Truby and J. A. Lewis, Printing soft matter in three dimensions, Nature (London) 540, 371 (2016).

[4] J. Christensen, M. Kadic, O. Kraft, and M. Wegener, Vibrant times for mechanical metamaterials, MRS Commun. 5, 453 (2015).

[5] K. Bertoldi, V. Vitelli, J. Christensen, and M. van Hecke, Flexible mechanical metamaterials, Nat. Rev. 2, 17066 (2017).

[6] J. N. Grima and K. E. Evans, Auxetic behavior from rotating squares, J. Mater. Sci. Lett. 19, 1563 (2000).

[7] Y. Cho, J.-H. Shin, A. Costa, T. A. Kim, V. Kunin, J. Li, S. Yeon Lee, S. Yang, H. N. Han, I.-S. Choi, and D. J. Srolovitz, Engineering the shape and structure of materials by fractal cut, Proc. Natl. Acad. Sci. U.S.A. 111, 17390 (2014).

[8] A. Clausen, F. Wang, J. S. Jensen, O. Sigmund, and J. A. Lewis, Topology optimized architectures with programmable poisson's ratio over large deformations, Adv. Mater. 27, 5523 (2015).

[9] R. S. Lakes, T. Lee, A. Bersie, and Y. C. Wang, Extreme damping in composite materials with negative-stiffness inclusions, Nature (London) 410, 565 (2001).

[10] L. B. Kashdan, M. R. Haberman, P. S. Wilson, and C. C. Seepersad, Constrained negative stiffness metamaterials, J. Acoust. Soc. Am. 128, 2428 (2010).

[11] L. Wu, B. Li, and J. Zhou, Isotropic negative thermal expansion metamaterials, ACS Appl. Mater. Interfaces 8, 17721 (2016).

[12] Q. Wang, J. A. Jackson, Q. Ge, J. B. Hopkins, C. M. Spadaccini, and N. X. Fang, Lightweight Mechanical Metamaterials with Tunable Negative Thermal Expansion, Phys. Rev. Lett. 117, 175901 (2016).

[13] B. Florijn, C. Coulais, and M. van Hecke, Programmable Mechanical Metamaterials, Phys. Rev. Lett. 113, 175503 (2014).

[14] S. Shan, S. H. Kang, J. R. Raney, P. Wang, L. Fang, F. Candido, J. A. Lewis, and K. Bertoldi, Multistable architected materials for trapping elastic strain energy, Adv. Mater. 27, 4296 (2015).

[15] B. Haghpanah, L. Salari-Sharif, P. Pourrajab, J. Hopkins, and L. Valdevit, Multistable shape-reconfigurable architected materials, Adv. Mater. 28, 7915 (2016).

[16] J. R. Raney, N. Nadkarni, C. Daraio, D. M. Kochmann, J. A. Lewis, and K. Bertoldi, Stable propagation of mechanical signals in soft media using stored elastic energy, Proc. Natl. Acad. Sci. U.S.A. 113, 9722 (2016).

[17] N. Nadkarni, A. F. Arrieta, C. Chong, D. M. Kochmann, and C. Daraio, Unidirectional Transition Waves in Bistable Lattices, Phys. Rev. Lett. 116, 244501 (2016).

[18] B. Deng, J. R. Raney, V. Tournat, and K. Bertoldi, Elastic Vector Solitons in Soft Architected Materials, Phys. Rev. Lett. 118, 204102 (2017).

[19] H. Yasuda, Y. Miyazawa, E. G. Charalampidis, C. Chong, P. G. Kevrekidis, and J. Yang, Origami-based impact mitigation via rarefaction solitary wave creation, Sci. Adv. 5, eaau2835 (2019).

[20] M. Taylor, L. Francesconi, M. Gerendás, A. Shanian, C. Carson, and K. Bertoldi, Low porosity metallic periodic structures with negative poissons ratio, Adv. Mater. 26, 2365 (2014).

[21] C. Coulais, C. Kettenis, and M. van Hecke, A characteristic length scale causes anomalous size effects and boundary programmability in mechanical metamaterials, Nat. Phys. 14, 40 (2018).

[22] R. K. Narisetti, M. Ruzzene, and M. J. Leamy, Study of wave propagation in strongly nonlinear periodic lattices using a harmonic balance approach, Wave Motion **49**, 394 (2012).

[23] A. Leonard, C. Chong, P. G. Kevrekidis, and C. Daraio, Traveling waves in 2d hexagonal granular crystal lattices, Granular Matter **16**, 531 (2014).

[24] H. A. Burgoyne, J. A. Newman, W. C. Jackson, and C. Daraio, Guided impact mitigation in 2d and 3d granular crystals, Procedia Eng. **103**, 52 (2015).

[25] S. Sen, T. R. Krishna Mohan, and M. Tiwari, Impact dispersion using 2D and 3D composite granular packing, KONA Powder Part. J. **34**, 248 (2017).

[26] J. A. Lewis, Direct ink writing of 3d functional materials, Adv. Funct. Mater. **16**, 2193 (2006).

[27] T. C. Chu, W. F. Ranson, and M. A. Sutton, Applications of digital-image-correlation techniques to experimental mechanics, Exp. Mech. **25**, 232 (1985).

[28] J. Blaber, B. Adair, and A. Antoniou, Ncorr: Open-source 2d digital image correlation matlab software, Exp. Mech. **55**, 1105 (2015).

[29] See Supplemental Material at http://link.aps.org/supplemental/10.1103/PhysRevLett.123.024101 for additional details about experimental, numerical, and analytical results.

[30] A. Spadoni and C. Daraio, Generation and control of sound bullets with a nonlinear acoustic lens, Proc. Natl. Acad. Sci. U.S.A. **107**, 7230 (2010).

[31] C. M. Donahue, P. W. J. Anzel, L. Bonanomi, T. A. Keller, and C. Daraio, Experimental realization of a nonlinear acoustic lens with a tunable focus, Appl. Phys. Lett. **104**, 014103 (2014).

[32] K. Li, P. Rizzo, and X. Ni, Alternative designs of acoustic lenses based on nonlinear solitary waves, J. Appl. Mech. **81**, 071011 (2014).

[33] B. Deng, P. Wang, Q. He, V. Tournat, and K. Bertoldi, Metamaterials with amplitude gaps for elastic solitons, Nat. Commun. **9**, 3410 (2018).

[34] B. Deng, V. Tournat, and K. Bertoldi, Effect of predeformation on the propagation of vector solitons in flexible mechanical metamaterials, Phys. Rev. E **98**, 053001 (2018).

[35] A. Polyanin and V. Zaitsev, *Handbook of Nonlinear Partial Differential Equations*, 2nd ed. (Chapman and Hall/CRC, Boca Raton-London-New York, 2011).

[36] A.-M. Wazwaz, New solitons and kink solutions for the Gardner equation, Commun. Nonlinear Sci. Numer. Simul. **12**, 1395 (2007).

Supporting Information for
Focusing and Mode Separation of Elastic Vector Solitons in a 2D Soft Mechanical Metamaterial

January 24, 2019

S1 Experiments

S1.1 Fabrication

In this work, we consider a metamaterial comprising a two dimensional (2D) array of counter-rotating hinged squares (*1–5*), all made of elastomeric material (polydimethylsiloxane - PDMS). The 2D system is circular, with 30 unit squares along its diameter (Fig. S1a). All squares are rotated by offset angles of $\theta_0 = 25°$ with respect to the horizontal and vertical directions, are connected to one another at their vertices, and have center-to-center-distance $a = 9.27$ mm (the pre-programmed shape is indicated as black lines in Fig. S1b). The sample was printed in the shape of a rectangular octagon using direct ink writing (*4, 6–8*), and subsequently cut into a circle using a laser cutter. Note that due to the finite acceleration of the print-head, the connections between the squares become somewhat rounded, with widths of approximately 5 mm (Fig. S1b). A thin strip of PDMS was then printed around the circumference of the circular system to constrain and couple the motion of the partial squares around the border, and steel spheres (4.76 mm in diameter) were embedded within the squares to increase the local inertia and decrease wave speed (no steel spheres were added to the partial squares along the

1

circumference). Finally, a speckle pattern was applied to the surface of the specimen by lightly spray painting with black paint to enhance the contrast for the Digital Image Correlation (DIC) analysis *(9)*.
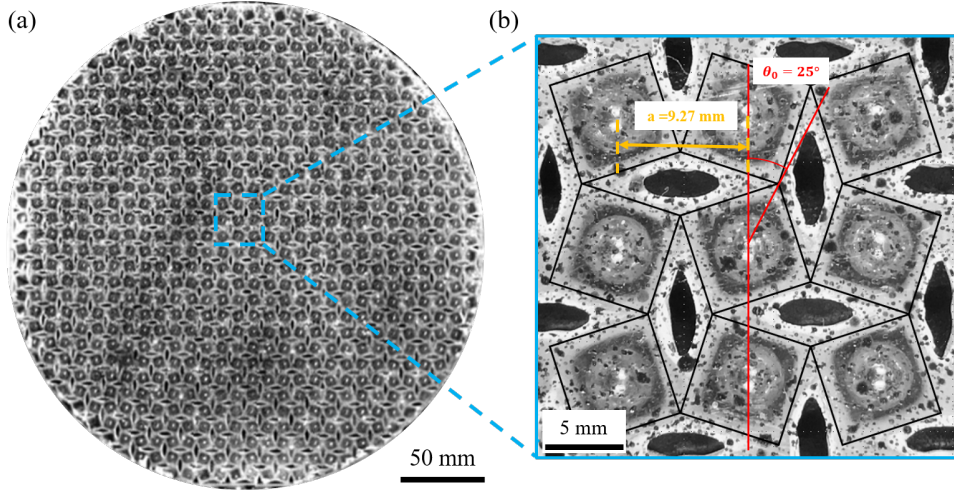

Figure S1: (a) Image of the 2D sample. (b) Magnified view, with the black lines indicating the pre-programmed path of the print-head (i.e., the ideal shape of the squares). The connections between the squares are not as sharp as intended because of the change of speed around corners during printing.

S1.2 Testing

To investigate the propagation of elastic pulses in the system, the specimen is first laid flat on a bed of closed packed steel spheres (to minimize friction), each with a diameter of 19 mm. An impulse is generated by an aluminum impactor with a 72 mm long flat end that spans the width of eight unit cells (Fig. S2). By impacting the sample at different locations along the circumference, we apply a displacement signal along different directions defined as

$$\hat{\mathbf{e}}_{||} = \cos\phi\,\hat{\mathbf{e}}_x + \sin\phi\,\hat{\mathbf{e}}_y, \tag{S1}$$

where $\hat{\mathbf{e}}_x$ and $\hat{\mathbf{e}}_y$ denote the two directions of periodicity of the system, and ϕ is the angle be-tween the normal to the impactor and $\hat{\mathbf{e}}_x$ (see Fig. S2). The impulse displacement is controlled by the initial gap distance between the impactor and the specimen, while its shape is determined

2

by the initial velocity applied to the impactor. The propagation of the pulse wave through the specimen is observed with a high-speed camera (Photron Mini AX-200) recording at 4000 Hz with a pixel size of 0.28 mm/pixel. 2D DIC analysis is then performed using an open source MATLAB-based software (*10*) with subset size of 12 pixels and a subset spacing of 6 pixels to obtain the full field displacement. Finally, the velocity is calculated from the displacement data using the 4-th order accurate central difference scheme.
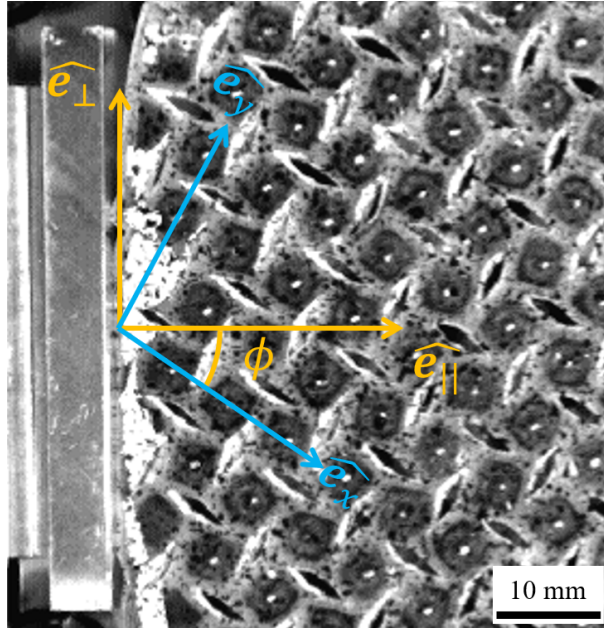

Figure S2: Magnified view of the sample, highlighting the impactor (on the left) and the impact direction $\hat{e}_{||}$.

S1.3 Experimental results

In Fig. S3, we show contours of the velocity components $v_{||} = v_x \cos\phi + v_y \sin\phi$ and $v_{\perp} = -v_x \sin\phi + v_y \cos\phi$ along $\hat{e}_{||}$ and $\hat{e}_{\perp}$, respectively (v_x and v_y being the velocity components along the x and y direction, respectively), obtained via DIC at t=3.5 and 5.5 ms for $\phi = 0°$, $15°$, $30°$ and $45°$ (the videos recorded during these experiments are shown in Movie S1). Moreover, in Fig. S4 we report the evolution of $v_{||}$ at t=3.5 and 5.5 ms as a function of the distance from
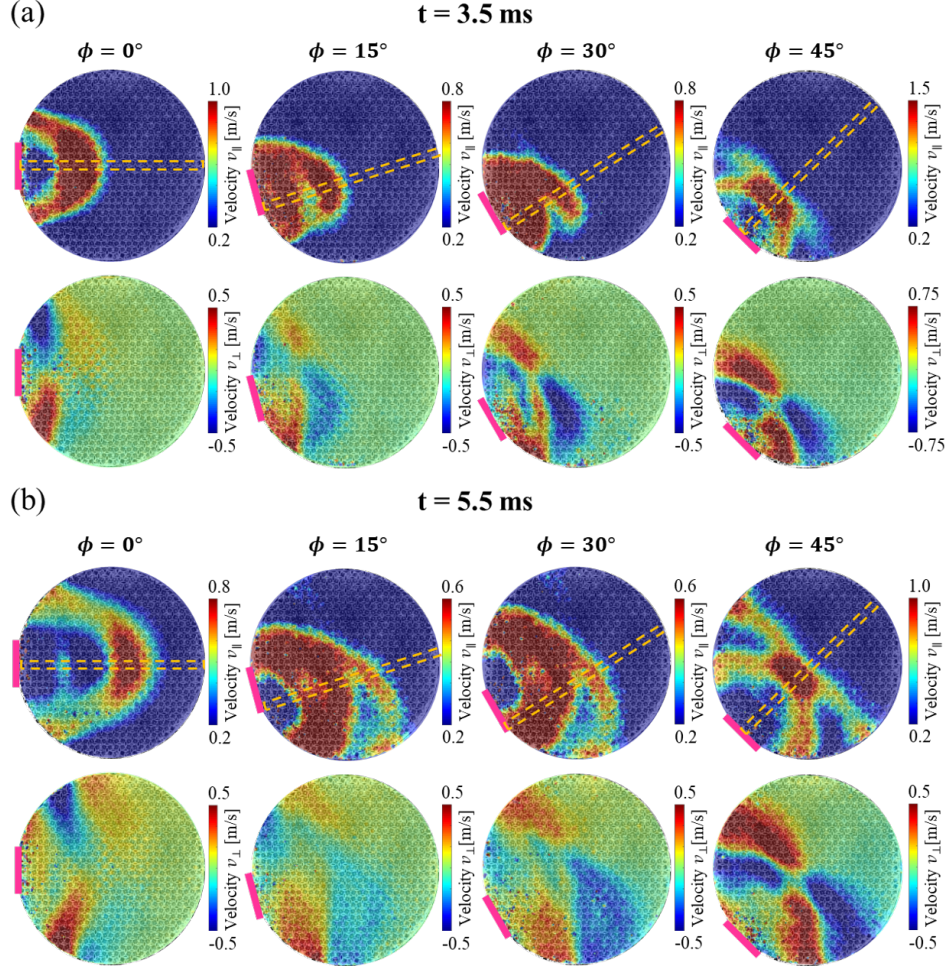
Figure S3: Contour plots of $v_{||}$ and $v_\perp$ for all impact angles at (a) $t = 3.5$ ms, (b) $t = 5.5$ ms. The magenta lines indicate the impactor. The full time evolution is available in Movie S1.

the impactor d along three lines perpendicular to the bottom, top, and center of the impactor. Finally, in Fig. S5 we report the spatial-temporal map of $v_{||}$, which at any given time t is calculated by taking the maximum value between those measured within a small window (with width delimited by the dashed yellow lines shown in Fig. S3). Note that the location of the small window is informed by the velocity contours of Fig. S3 as well as the plots of Fig. S4. Specifically, for $\phi = 15°$ and $30°$ the window is chosen near the bottom of the impactor to capture the distinct peaks of the faster and slower pulses in the velocity profile at $t = 5.5$ ms
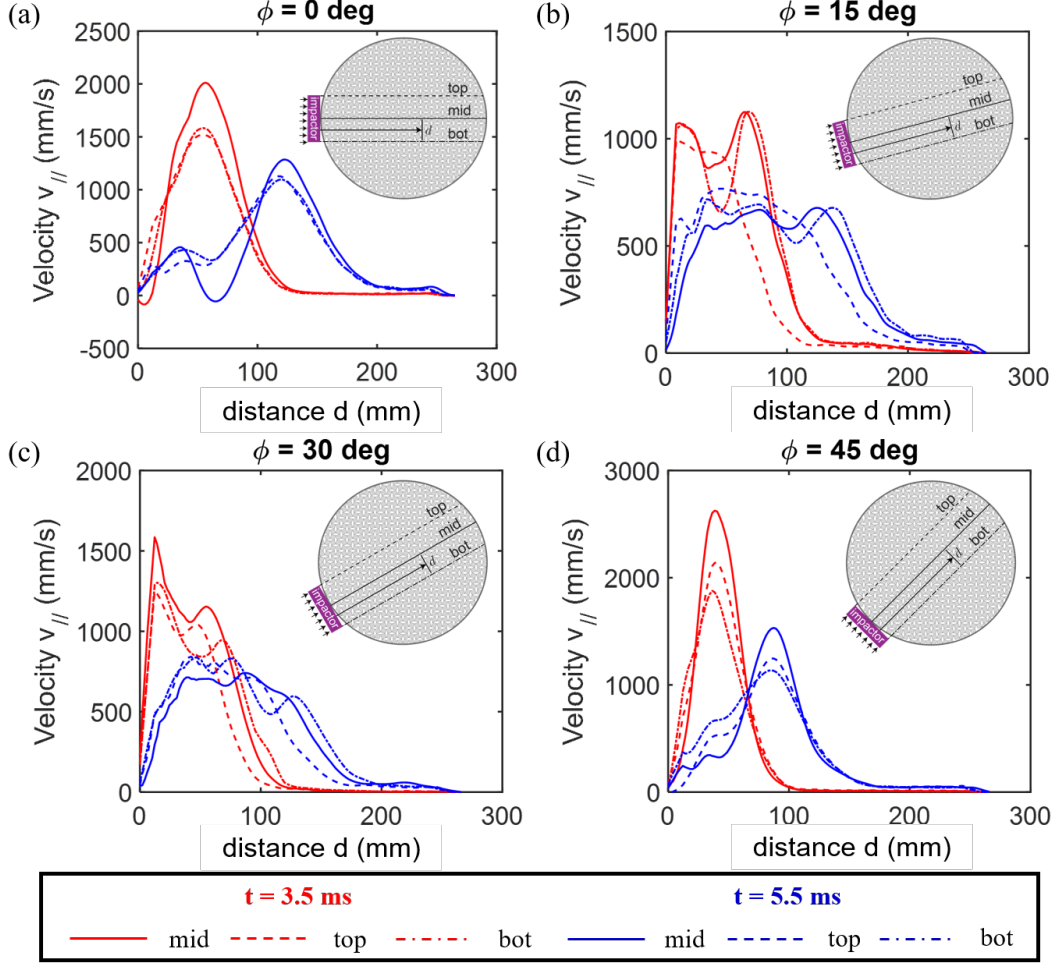
4

Figure S4: Evolution of $v_{\parallel}$ as a function of the distance from the impactor d at t=3.5 and 5.5. ms for (a) 0°, (b) $\phi = 15°$, (c) $\phi = 30°$ and (d) $\phi = 45°$.

(Fig. S4b and c). We use the plots of both Figs. S4 and S5 to extract the wave speed c, which corresponds to the peaks of the velocity profile.

$\underline{\phi = 0°}$. Though an impulse would typically disperse as it travels through a structure, for this system it is observed that for impacts along either principal axis pulses propagate through the 2D system maintaining both their shape and velocity (i.e., they propagate in a solitary fashion). Specifically, both Figs. S4a and S5a clearly indicate that for $\phi = 0°$ the velocity profile is characterized by a single peak with nearly constant width, from which the wave speed is extracted
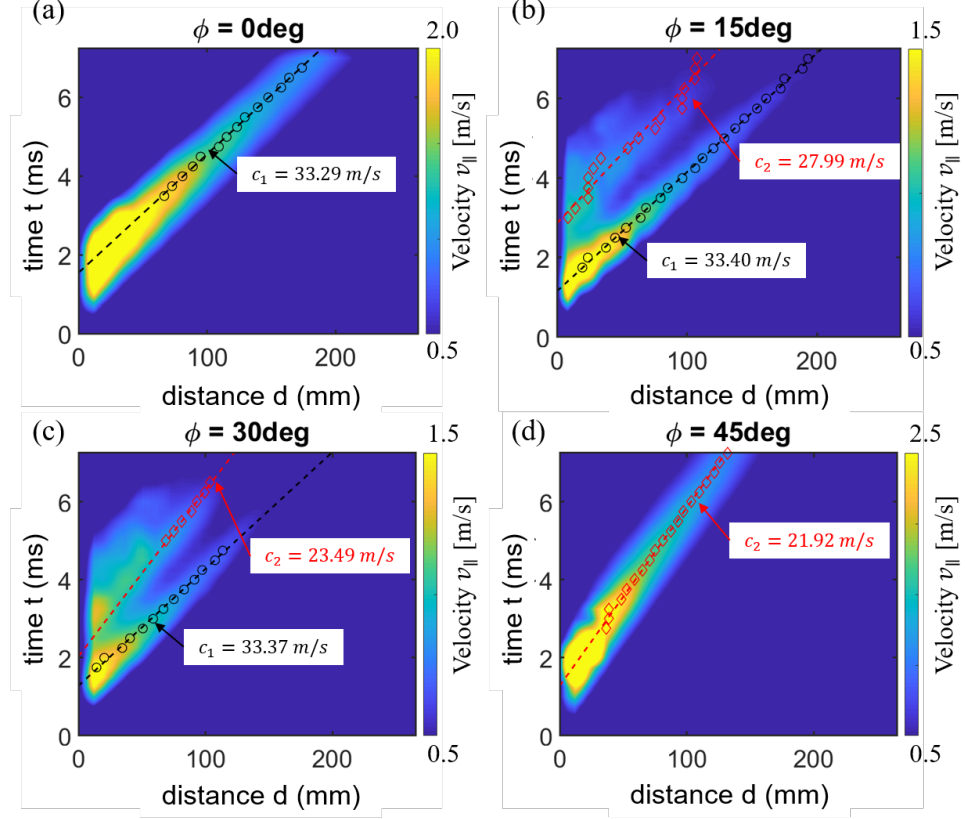
Figure S5: Spatial-temporal map of $v_{||}$ for (a) $\phi = 0°$, (b) $\phi = 15°$, (c) $\phi = 30°$, and (d) $\phi = 45°$

as 33.3 m/s.

<u>$\phi = 15°$ **and** $30°$</u>. Differently, we find that for $\phi = 15°$ and $30°$ the profile of $v_{||}$ immediately after the impact is asymmetric with respect to the propagation axis $\hat{e}_{||}$ (see contours at $t = 3.5$ ms in Fig. S3b). This asymmetry results from the underlying elastic anisotropy, which produces different soliton speeds along different directions of the structure. This leads to an apparent separation of pulses in some directions, an effect which becomes even more visible at later times (see contours at $t = 5.5$ ms in Fig. S3b). The separation of modes is also confirmed by the contours of the shear velocity, $v_{\perp}$, in Fig. S3. Specifically, the existence of both positive and negative shear velocities along the propagation direction indicates that the two pulse modes have different symmetries, and propagate at different wave speeds. This is not the case for $\phi = 0$,

6

where positive and negative shear velocity pulses are symmetric relative to $\hat{e}_{\parallel}$ and propagate at the same speed - indicating that the same mode is excited with opposite polarization on each side of the propagation axis. Finally, the wave speed of the two modes for both $\phi = 15°$ and $30°$ can be extracted from Fig. S5b and c. For $\phi = 15°$, the faster pulse propagates at 33.4 m/s while the slower pulse propagates at 28.0 m/s. For $\phi = 30°$, the faster pulse propagates at 33.4 m/s while the slower pulse propagates at 23.5 m/s.

$\underline{\phi = 45°}$. The velocity profiles for $\phi = 45°$ indicate that there is again only one wave mode travelling through the system along the $\hat{e}_{\parallel}$ direction with a speed of 21.9 m/s. While a single pulse was also observed for $\phi = 0°$, the wave fronts for $\phi = 0°$ and $45°$ are very different. For $\phi = 0°$ the wave front maintains its width in the $\hat{e}_{\parallel}$ direction during propagation, but becomes more disperse in the $\hat{e}_{\perp}$ direction. By contrast, for $\phi = 45°$, the pulse keeps its shape in both $\hat{e}_{\parallel}$ and $\hat{e}_{\perp}$ directions. As a matter of fact, the pulse transversal width in Fig. S3b is the same as the impactor width. This suggests that for $\phi = 45°$ the wave has a transversal self focusing effect, balancing the linear beam diffraction and stabilizing the pulse lateral width. This potentially leads to the generation of compact sound bullets of very large amplitudes, which may dramatically impact a variety of applications, such as biomedical devices, nondestructive evaluation, and defense systems. To better quantify this observed absence of divergence, in Figs. S6a and b we report the evolution of $v_{\parallel}$ in a small window (delimited by the dashed red lines shown in Fig. S6c) oriented along the $\hat{e}_{\perp}$ direction at $t = 4, 5$ and 6 ms for $\phi = 0°$ and $45°$, respectively. Note that at each time t the window is located at the pulse front, with the distance d from the impactor extracted from Fig. S5a and d. The plots clearly indicate that the width of the wave front for $\phi = 0°$ grows wider during propagation, while remaining roughly constant for $\phi = 45°$. This effect can be quantified by inspecting the time evolution of transversal width $W_{\perp}$ (see S6d), which corresponds to the full width at half maximum (FWHM) of the velocity profiles plotted in Figs. S6a and b. We find that the variation in width for $\phi = 45°$ is significantly

7

smaller relative to that observed for $\phi = 0°$, confirming the self focusing effect observed in the contour plots of Fig. S3.
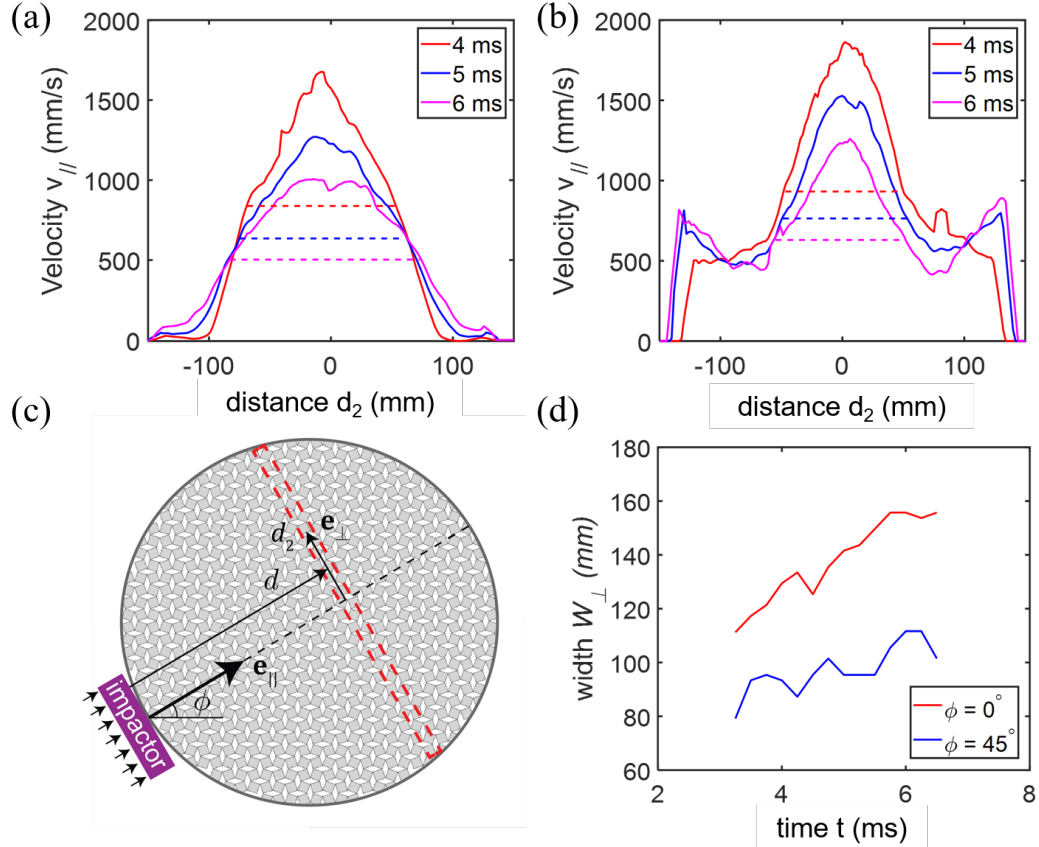

Figure S6: Evolution of $v_{||}$ in a small window (delimited by the dashed red lines shown in c) oriented along the $\hat{e}_\perp$ direction at $t=$ 4, 5 and 6 ms for (a) $\phi = 0°$ and (b) $\phi = 45°$. The dashed lines indicate the full width at half maximum of the velocity profiles. (c) Schematic indicating the window in which we monitor $v_{||}$. (d) Time evolution of the width $W_\perp$, which corresponds to the full width at half maximum of the velocity profiles.

S2   Mathematical model

As recently shown in several studies (*4, 5, 11*), the response of the system considered here can be accurately captured by modeling it as an array of rigid bodies connected at the vertices via a combination of longitudinal and rotational linear springs. However, in all previous efforts only deformations along one of its principal directions of symmetry (i.e., one of the two directions of periodicity of the structure) were considered. As such, only two degrees of freedom (i.e., longitudinal displacement and rotation) were assigned to each rigid unit. By contrast, here we derive the discrete model and the corresponding analytical solution for planar waves for the general 2D case in which the waves propagate along arbitrary directions.

S2.1   Discrete model

In our discrete model we consider the squares to be rigid and to have three degrees of freedom: the displacement in the x-direction, u_x, the displacement in the y-direction, u_y, and the rotation around the z-axis, θ. Moreover, to facilitate the analysis, we define the positive direction of rotation alternatively for neighboring squares. Specifically, for each square we assume the energetically favorable direction of rotation under compression to be the positive one. As such, for the $[i,\,j]$-th unit (which is rotated by θ_0 in a clockwise direction - see Fig. S7-c) a clockwise rotation is positive (see blue arrow in Fig. S7-c), while for the $[i-1,\,j]$-th, $[i+1,\,j]$-th, $[i,\,j-1]$-th and $[i,\,j+1]$-th units (which are rotated by θ_0 in a counter-clockwise direction - see Fig. S7-c), counterclockwise rotations are considered positive (see purple arrow in Fig. S7-c).

As for the hinges, we model them using a combination of three linear springs: (i) their longitudinal response is captured by a spring with stiffness k_l; (ii) their shearing is governed by a spring with stiffness k_s; (iii) their bending is captured by a torsional spring with stiffness k_θ.

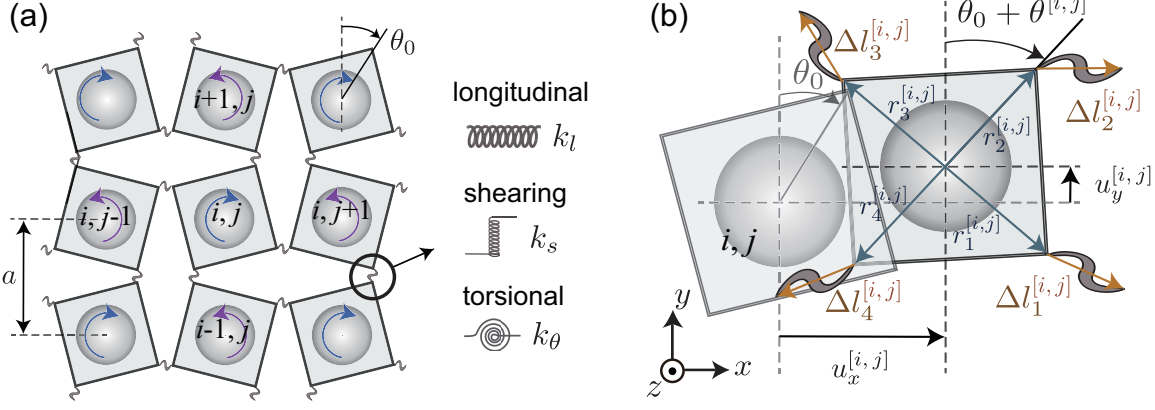Under the assumptions listed above, the equations of motion for the $[i,\,j]$-th square are given

9

Figure S7: (a) Discrete model based on rigid units connected at their vertices by springs. (b) Schematic of the $[i,\,j]$-th rigid square unit.

by

$$m\ddot{u}_x = \sum_{p=1}^{4} F_p^{x\,[i,j]},$$

$$m\ddot{u}_y = \sum_{p=1}^{4} F_p^{y\,[i,j]}, \qquad (S2)$$

$$J\ddot{\theta} = \sum_{p=1}^{4} M_p^{[i,j]},$$

where m and J are the mass and moment of inertia of the rigid unit, which are measured as 0.797 g and 5.457 g·mm² respectively. Moreover, $F_p^{x\,[i,j]}$ and $F_p^{y\,[i,j]}$ are the forces in the x-direction and the y-direction generated at the p-th vertex of the $[i,\,j]$-th unit by the springs and $M_p^{[i,j]}$ represents the corresponding moment. For a square initially rotated by an angle θ_0, these forces and moments are given by

$$F_p^{x\,[i,j]} = \mathbf{k}_p \cdot \mathbf{\Delta l}_p^{[i,j]} \cdot \hat{\mathbf{e}}_x,$$

$$F_p^{y\,[i,j]} = \mathbf{k}_p \cdot \mathbf{\Delta l}_p^{[i,j]} \cdot \hat{\mathbf{e}}_y, \qquad (S3)$$

$$M_p^{[i,j]} = -k_\theta \Delta\theta_p^{[i,j]} - \left\| \mathbf{r}_p^{[i,j]}(\theta^{[i,j]}) \times \left(\mathbf{k}_p \cdot \mathbf{\Delta l}_p^{[i,j]} \right) \right\|,$$

with

$$\mathbf{k}_p = \begin{bmatrix} k_l & 0 \\ 0 & k_s \end{bmatrix}, \quad \text{for } p = 1, 3, \qquad (S4)$$

10

and

$$\mathbf{k}_p = \begin{bmatrix} k_s & 0 \\ 0 & k_l \end{bmatrix}, \quad \text{for } p = 2, 4. \tag{S5}$$

Furthermore, $\Delta\theta_p^{[i,j]}$ is the change in angle experienced by the rotational spring connected to the p-th vertex of the $[i, j]$-th rigid unit

$$
\begin{aligned}
\Delta\theta_1^{[i,j]} &= \theta^{[i,j]} + \theta^{[i,j+1]}, \\
\Delta\theta_2^{[i,j]} &= \theta^{[i,j]} + \theta^{[i+1,j]}, \\
\Delta\theta_3^{[i,j]} &= \theta^{[i,j]} + \theta^{[i,j-1]}, \\
\Delta\theta_4^{[i,j]} &= \theta^{[i,j]} + \theta^{[i-1,j]},
\end{aligned}
\tag{S6}
$$

and $\mathbf{r}_p^{[i,j]}$ denotes the vector that connects the center of the $[i, j]$-th rigid unit to its p-th vertex (see Fig. S7-c)

$$
\begin{aligned}
\mathbf{r}_1^{[i,j]}(\theta^{[i,j]}) &= \frac{a}{2\cos\theta_0} \left[\mathcal{C}(\theta^{[i,j]}), \; (-1)^{i+j}\mathcal{S}(\theta^{[i,j]}) \right], \\
\mathbf{r}_2^{[i,j]}(\theta^{[i,j]}) &= \frac{a}{2\cos\theta_0} \left[-(-1)^{i+j}\mathcal{S}(\theta^{[i,j]}), \; \mathcal{C}(\theta^{[i,j]}) \right], \\
\mathbf{r}_3^{[i,j]}(\theta^{[i,j]}) &= -\frac{a}{2\cos\theta_0} \left[\mathcal{C}(\theta^{[i,j]}), \; (-1)^{i+j}\mathcal{S}(\theta^{[i,j]}) \right], \\
\mathbf{r}_4^{[i,j]}(\theta^{[i,j]}) &= \frac{a}{2\cos\theta_0} \left[(-1)^{i+j}\mathcal{S}(\theta^{[i,j]}), \; -\mathcal{C}(\theta^{[i,j]}) \right],
\end{aligned}
\tag{S7}
$$

with

$$\mathcal{C}(\theta^{[i,j]}) = \cos\left(\theta^{[i,j]} + \theta_0\right), \quad \mathcal{S}(\theta^{[i,j]}) = \sin\left(\theta^{[i,j]} + \theta_0\right), \tag{S8}$$

where a is the center-to-center distance between two neighboring units. Finally, $\mathbf{\Delta l}_p^{[i,j]}$ is a vector whose entries provide the change in length along the x- and y- directions of the linear springs connected to the p-th vertex,

$$
\begin{aligned}
\mathbf{\Delta l}_1^{[i,j]} &= \left(u_x^{[i,j+1]} - u_x^{[i,j]} \right) \hat{\mathbf{e}}_x + \left(u_y^{[i,j+1]} - u_y^{[i,j]} \right) \hat{\mathbf{e}}_y + \mathbf{\Delta r}_3^{[i,j+1]} - \mathbf{\Delta r}_1^{[i,j]}, \\
\mathbf{\Delta l}_2^{[i,j]} &= \left(u_x^{[i+1,j]} - u_x^{[i,j]} \right) \hat{\mathbf{e}}_x + \left(u_y^{[i+1,j]} - u_y^{[i,j]} \right) \hat{\mathbf{e}}_y + \mathbf{\Delta r}_4^{[i+1,j]} - \mathbf{\Delta r}_2^{[i,j]}, \\
\mathbf{\Delta l}_3^{[i,j]} &= \left(u_x^{[i,j-1]} - u_x^{[i,j]} \right) \hat{\mathbf{e}}_x + \left(u_y^{[i,j-1]} - u_y^{[i,j]} \right) \hat{\mathbf{e}}_y + \mathbf{\Delta r}_1^{[i,j-1]} - \mathbf{\Delta r}_3^{[i,j]}, \\
\mathbf{\Delta l}_4^{[i,j]} &= \left(u_x^{[i-1,j]} - u_x^{[i,j]} \right) \hat{\mathbf{e}}_x + \left(u_y^{[i-1,j]} - u_y^{[i,j]} \right) \hat{\mathbf{e}}_y + \mathbf{\Delta r}_2^{[i-1,j]} - \mathbf{\Delta r}_4^{[i,j]},
\end{aligned}
\tag{S9}
$$

11

with

$$\mathbf{\Delta r}_p^{[i,j]} = \mathbf{r}_p^{[i,j]}(\theta^{[i,j]}) - \mathbf{r}_p^{[i,j]}(0). \tag{S10}$$

Substitution of Eqs. (S3)-(S10) into Eq. (S2), yields the expanded governing equation

$$
\begin{aligned}
\frac{\partial^2 u_x^{[i,j]}}{\partial t^2} =& k_l \left(u_x^{[i,j+1]} + u_x^{[i,j-1]} - 2u_x^{[i,j]} \right) + k_s \left(u_x^{[i+1,j]} + u_x^{[i-1,j]} - 2u_x^{[i,j]} \right) \\
& - \frac{k_l a}{2\cos\theta_0} \left[\cos(\theta^{[i,j+1]} + \theta_0) - \cos(\theta^{[i,j-1]} + \theta_0) \right] \\
& + (-1)^{i+j} \frac{k_s a}{2\cos\theta_0} \left[\sin(\theta^{[i+1,j]} + \theta_0) - \sin(\theta^{[i-1,j]} + \theta_0) \right] \\
\frac{\partial^2 u_y^{[i,j]}}{\partial t^2} =& k_l \left(u_y^{[i+1,j]} + u_y^{[i-1,j]} - 2u_y^{[i,j]} \right) + k_s \left(u_y^{[i,j+1]} + u_y^{[i,j-1]} - 2u_y^{[i,j]} \right) \\
& - \frac{k_l a}{2\cos\theta_0} \left[\cos(\theta^{[i+1,j]} + \theta_0) - \cos(\theta^{[i-1,j]} + \theta_0) \right] \\
& - (-1)^{i+j} \frac{k_s a}{2\cos\theta_0} \left[\sin(\theta^{[i,j+1]} + \theta_0) - \sin(\theta^{[i,j-1]} + \theta_0) \right] \\
\frac{\partial^2 \theta^{[i,j]}}{\partial t^2} =& - k_\theta \left(\theta^{[i+1,j]} + \theta^{[i-1,j]} + \theta^{[i,j+1]} + \theta^{[i,j-1]} + 4\theta^{[i,j]} \right) - \frac{k_l a^2}{4\cos^2\theta_0} \sin(\theta^{[i,j]} + \theta_0) \\
& \times \left[8\cos\theta_0 - \cos(\theta^{[i+1,j]} + \theta_0) - \cos(\theta^{[i-1,j]} + \theta_0) - \cos(\theta^{[i,j+1]} + \theta_0) \right. \\
& - \cos(\theta^{[i,j-1]} + \theta_0) - 4\cos(\theta^{[i,j]} + \theta_0) + \frac{2k_l \cos^2\theta_0}{a} \left(u^{[i,j+1]} - u^{[i,j-1]} + v^{[i+1,j]} \right. \\
& \left. - v^{[i-1,j]} \right) \right] + \frac{k_s a^2}{4\cos^2\theta_0} \cos(\theta^{[i,j]} + \theta_0) \left[\sin(\theta^{[i,j+1]} + \theta_0) + \sin(\theta^{[i,j-1]} + \theta_0) \right. \\
& + \sin(\theta^{[i+1,j]} + \theta_0) + \sin(\theta^{[i-1,j]} + \theta_0) - 4\sin(\theta^{[i,j]} + \theta_0) \right] \\
& + (-1)^{i+j} \frac{2k_l \cos\theta_0}{a} \cos(\theta_0) \left(-u_x^{[i+1,j]} + u_x^{[i-1,j]} + u_y^{[i,j+1]} - u_y^{[i,j-1]} \right) \right]
\end{aligned}
$$
$$\tag{S11}$$

For a metamaterial comprising N hinged units Eqs. (S11) result in a system of $3N$ coupled differential equations, which we numerically solve using the 4th order Runge-Kutta method (via the Matlab function ode45). In Fig. S8 we report numerical results obtained by simulating the experiments considered in Figs. S2 and S3. Specifically, our numerical model comprises 716 square units arranged to form a circular structure with 30 squares along the diameter (see Figs. S8a). The squares have $\theta_0 = 25°$, $m = 0.797$ g, $J = 5.457$ g·mm^2, and center-to-center

distance $a = 9.27$ mm, and are connected via springs with $k_l = 16360$ N/m, $k_s = 8180$ N/m, and $k_\theta = 0.0312$ N·m/rad (note that the value for k_l is obtained by matching the numerically predicted pulse velocity with that extracted from the experiments of Fig. S5a, while the values for k_s and k_θ are those previously used in (11) and (4), respectively). Moreover, we excite the propagation of non-linear waves by applying the experimentally-extracted displacement of a point next to the center of the impactor (see Fig. S8b) to the squares on the boundary that are highlighted in magenta in Figs. S8c and e. Finally, to model the effect of the thin strip of PDMS printed along the circumference of the sample, we impose $\theta^{[i,j]} = 0$ to all other squares on the boundary, while leaving u_x and u_y unset. In Figs. S8c and e we show the contours of $v_\parallel$ and $v_\perp$ at $t = 6.5$ ms for $\phi = 0°$, 15°, 30° and 45°. Moreover, in Fig. S8d we report the spatial-temporal map of $v_\parallel$, calculated as described in Section S1.3. As in the experiments, we find that (*i*) the excitation results in soliton-like pulses propagating through the structure; (*ii*) for $\phi = 15°$ and 30° the wave seems to separate into two modes with different wave speeds (similar to the experiments); (*iii*) for $\phi = 45°$ the pulse has a transversal self-focusing effect and maintains its shape in both $\hat{e}_\parallel$ and $\hat{e}_\perp$ directions.

Having found that our discrete model closely matches the experimental results, we then use it to further investigate the response of the system, focusing on the effect of both size and loading conditions. We start by simulating a larger circular model comprising 2828 squares (see Fig. S9). When subjected to the initial and boundary conditions used to generate the results shown in Fig. S8, we find that the physical phenomena previously observed (i.e. soliton-like pulses, mode separation for $\phi = 15°$ and 30°, and self-focusing for $\phi = 45°$) not only persist, but are further accentuated. In particular, in Fig. S10 we concentrate on the self focusing effect and report the evolution of $v_\parallel$ as a function of the distance from the center of the impactor at $t=8$, 10 and 12 ms for $\phi = 0°$ (see Fig. S10a) and 45° (see Fig. S10b). Just as in the experiments (see Fig. S6), we find that for $\phi = 0°$ the width of the wave front grows wider during propagation,

while for $\phi = 45°$ it remains roughly constant - an observation that is further confirmed by the evolution of the $W_\perp$ over time (see Fig. S10c).

Finally, we use numerical analyses to make sure that the short width of the impactor used in our experiments does not play an important role. To this end, we consider a square domain comprising 60×60 squares and initiate planar waves by applying the displacement signal of Fig. S8b to an entire edge (i.e. to the squares highlighted in magenta in Fig. S11), while imposing $\theta = 0$ to all other squares on the boundary. The results reported in Fig. S11 indicate that the excitation initiates a soliton-like pulse for all considered angles ϕ and that for $\phi = 15°$ and $30°$ the pulse separates into two modes (the self-focusing effect previously found for $\phi = 45°$ is not observed given the planar nature of the initiated wave). As such, the numerical results of Figs. S9-S11 indicate that the phenomena observed in the experiments are not artifacts introduced by edge effects and boundary conditions, but rather emerge because of the bulk properties of the medium.
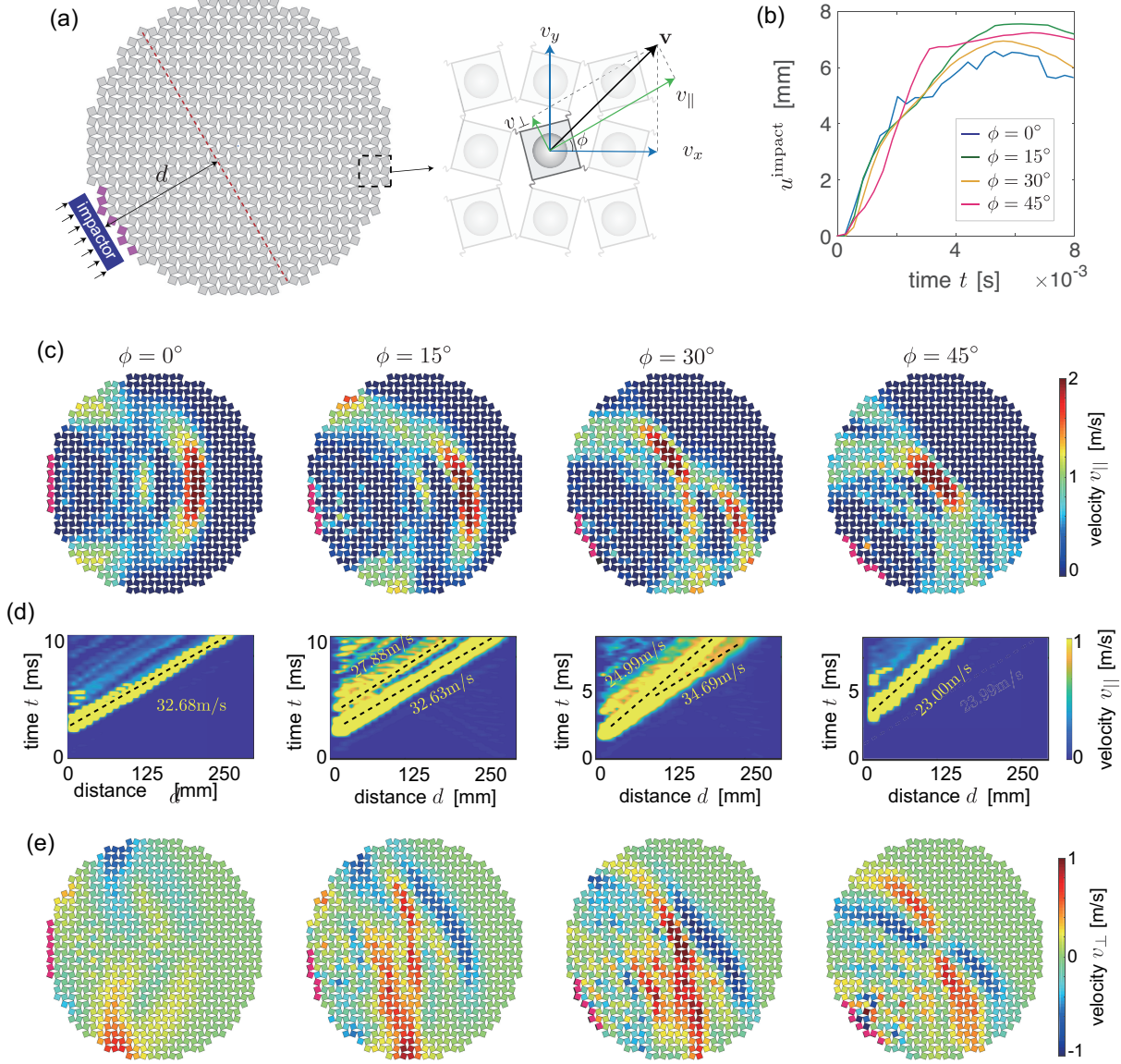
Figure S8: (a) Schematic of the circular model comprising 716 squares. (b) Experimentally-extracted displacement applied by the impactor to a point of the specimen next to the impactor's center. (c) Contour plots of $v_{\parallel}$ for all considered impact angles at $t = 6.5$ ms. (d) Spatial-temporal map of $v_{\parallel}$ for all considered impact angles. (e) Contour plots of $v_{\perp}$ for all considered impact angles at $t = 6.5$ ms. The magenta squares in (c) and (e) are those to which the displacement is applied. The full time evolution is available in Movie S2.
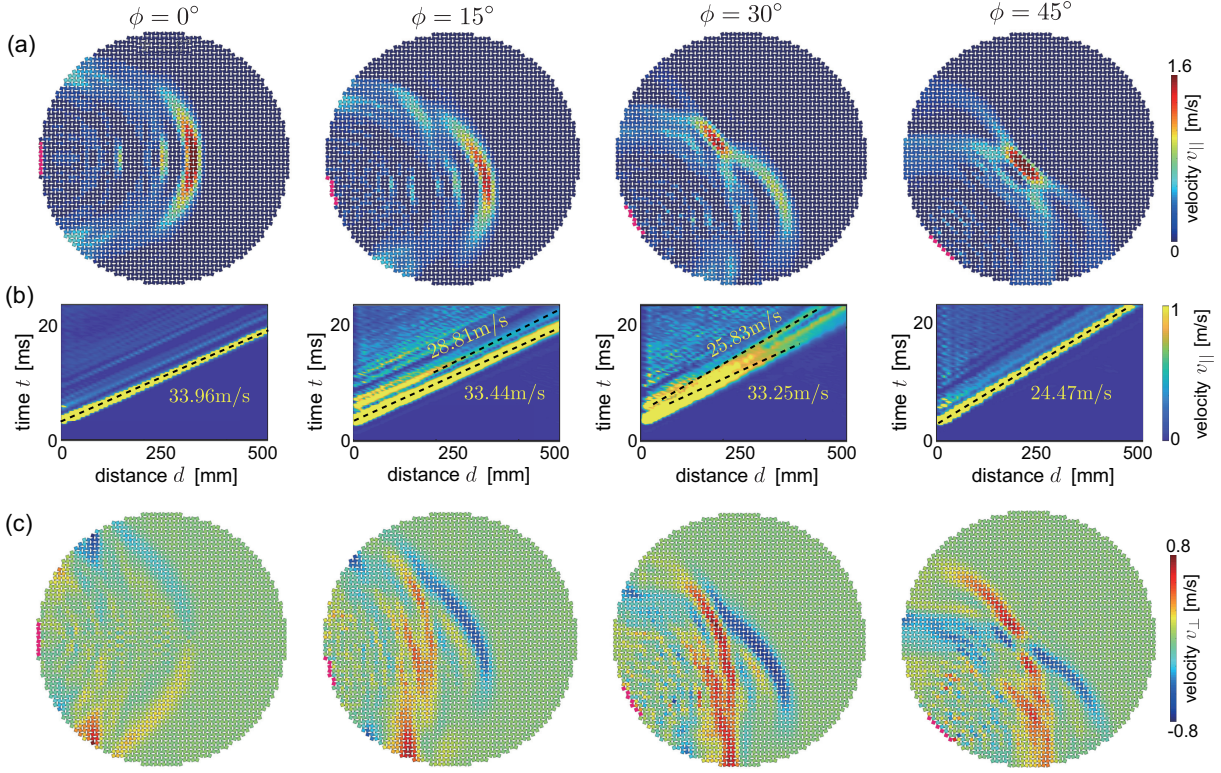
15

Figure S9: Numerical results for a circular model comprising 2828 squares. (a) Contour plots of $v_\parallel$ for all considered impact angles at $t = 12$ ms. (b) Spatial-temporal map of $v_\parallel$ for all considered impact angles. (c) Contour plots of $v_\perp$ for all considered impact angles at $t = 12$ ms. The magenta squares in (a) and (c) are those to which the displacement is applied. The full time evolution is available in Movie S2.
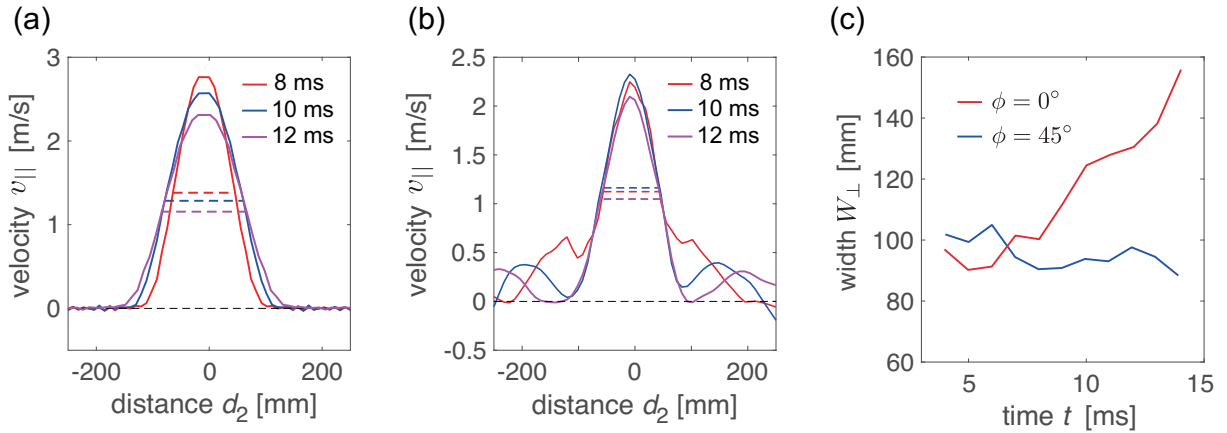

Figure S10: Evolution of $v_\parallel$ in a small window (delimited by the dashed red lines shown in Fig. S6c) oriented along the $\hat{\mathbf{e}}_\perp$ direction at $t = 8$, 10 and 12 ms for (a) $\phi = 0°$ and (b) $\phi = 45°$. The dashed lines indicate the full width at half maximum of the velocity profiles. (c) Time evolution of the full width at half maximum (FWHM) obtained from the velocity profiles.
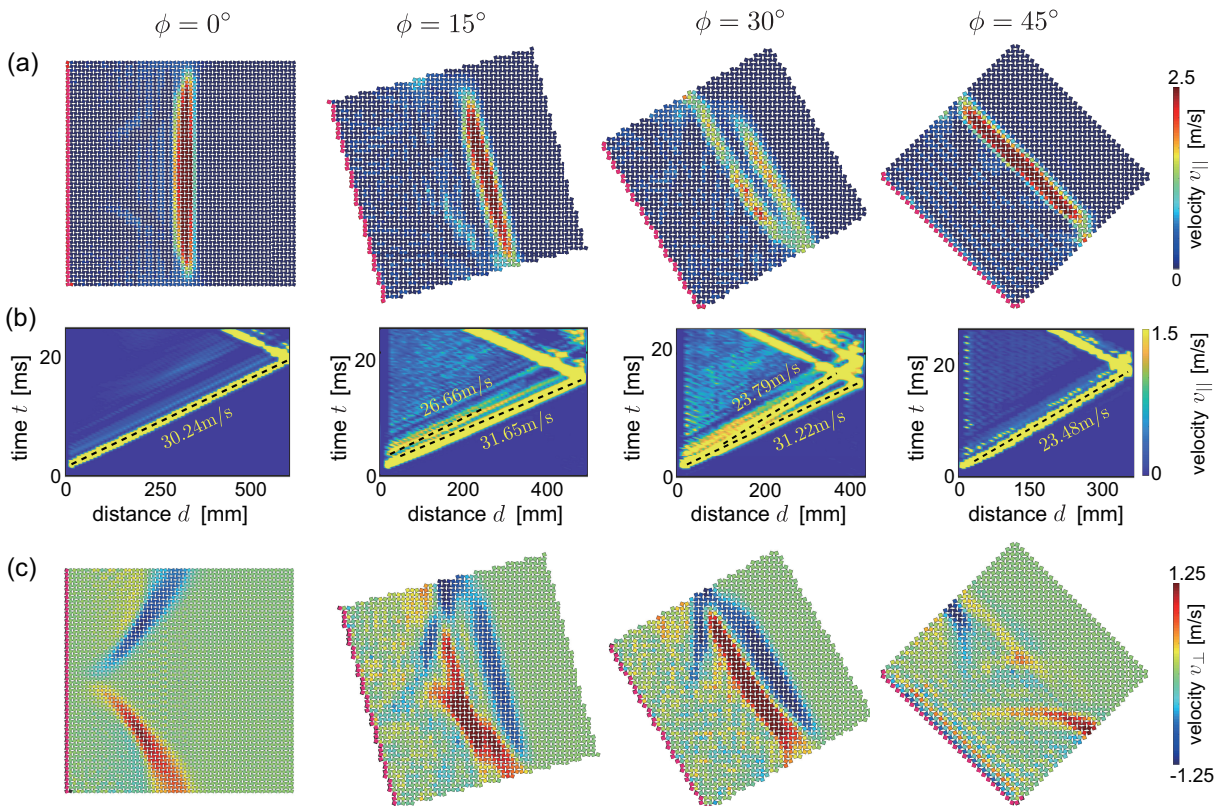
16

Figure S11: Numerical results for a square model comprising 60×60 squares. (a) Contour plots of $v_{||}$ for all considered impact angles at $t = 10$ ms. (b) Spatial-temporal map of $v_{||}$ for all considered impact angles. (c) Contour plots of $v_{\perp}$ for all considered impact angles at $t = 10$ ms. The magenta squares in (a) and (c) are those to which the displacement is applied. The full time evolution is available in Movie S2.

17

S2.2 Continuum model

Sice the numerical results of Fig. S11 reveal that the phenomena observed in our experiments emerge also when planar waves propagate in samples of large size, we next simplify Eqs. (S11) to derive analytical solutions for the case of planar waves. To this end, we first introduce three continuous functions u_x, u_y and θ, which interpolate the discrete variables $u_x^{[i,j]}$, $u_y^{[i,j]}$ and $\theta^{[i,j]}$ as

$$u_x\left(x = x^{[i,j]},\, y = y^{[i,j]}\right) = u_x^{[i,j]},$$
$$u_y\left(x = x^{[i,j]},\, y = y^{[i,j]}\right) = u_y^{[i,j]}, \tag{S12}$$
$$\theta\left(x = x^{[i,j]},\, y = y^{[i,j]}\right) = \theta^{[i,j]}$$

Assuming that the width of the propagating waves is much larger than the unit cell, the displacements u_x and u_y and the rotation θ of the $[i,\, j-1]$-th, $[i,\, j+1]$-th, $[i-1,\, j]$-th, and $[i+1,\, j]$-th units can then be expressed using Taylor expansion as

$$u_x\left(x^{[i+p,\,j]},\, y^{[i,\,j]},\, t\right) \approx \left[u_x + a\,p\,\partial_x u_x + \frac{(a\,p)^2}{2}\partial_{xx}u_x + \frac{(a\,p)^3}{6}\partial_{xxx}u_x\right]_{x^{[i,j]},\,y^{[i,j]},\,t}$$

$$u_x\left(x^{[i,\,j+p]},\, y^{[i,\,j]},\, t\right) \approx \left[u_x + a\,p\,\partial_y u_x + \frac{(a\,p)^2}{2}\partial_{yy}u_x + \frac{(a\,p)^3}{6}\partial_{yyy}u_x\right]_{x^{[i,j]},\,y^{[i,j]},\,t}$$

$$u_y\left(x^{[i+p,\,j]},\, y^{[i,\,j]},\, t\right) \approx \left[u_y + a\,p\,\partial_x u_y + \frac{(a\,p)^2}{2}\partial_{xx}u_y + \frac{(a\,p)^3}{6}\partial_{xxx}u_y\right]_{x^{[i,j]},\,y^{[i,j]},\,t}$$

$$u_y\left(x^{[i,\,j+p]},\, y^{[i,\,j]},\, t\right) \approx \left[u_y + a\,p\,\partial_y u_y + \frac{(a\,p)^2}{2}\partial_{yy}u_y + \frac{(a\,p)^3}{6}\partial_{yyy}u_y\right]_{x^{[i,j]},\,y^{[i,j]},\,t} \tag{S13}$$

$$\theta\left(x^{[i+p,\,j]},\, y^{[i,\,j]},\, t\right) \approx \left[\theta + a\,p\,\partial_x\theta + \frac{(a\,p)^2}{2}\partial_{xx}\theta + \frac{(a\,p)^3}{6}\partial_{xxx}\theta\right]_{x^{[i,j]},\,y^{[i,j]},\,t}$$

$$\theta\left(x^{[i,\,j+p]},\, y^{[i,\,j]},\, t\right) \approx \left[\theta + a\,p\,\partial_y\theta_y + \frac{(a\,p)^2}{2}\partial_{yy}\theta + \frac{(a\,p)^3}{6}\partial_{yyy}\theta\right]_{x^{[i,j]},\,y^{[i,j]},\,t}$$

where $p = -1,\, 1$ and $\partial_\alpha f = \partial f/\partial\alpha$. Moreover, if we assume that $\theta \ll 1$, $\sin(\theta_0 + \theta)$ and $\cos(\theta_0 + \theta)$ can be approximated as

$$\sin(\theta_0 + \theta) \approx \sin\theta_0 + \theta\,\cos\theta_0 - \theta^2\frac{\sin\theta_0}{2} - \theta^3\frac{\cos\theta_0}{6},$$
$$\cos(\theta_0 + \theta) \approx \cos\theta_0 - \theta\,\sin\theta_0 - \theta^2\frac{\cos\theta_0}{2} + \theta^3\frac{\sin\theta_0}{6}. \tag{S14}$$

18

Substitution of Eqs. (S13) and (S14) into Eq. (S11) yields

$$
m\ddot{u}_x = a^2 \left[k_l \partial_{xx} u_x + k_s \partial_{yy} u_x + \frac{\tan \theta_0 \, a^2 k_l}{6} \, \partial_{xxx}\theta + k_l \left(\tan \theta_0 + \theta - \tan \theta_0 \, \theta^2/2 \right) \partial_x \theta \right],
$$
$$
m\ddot{u}_y = a^2 \left[k_s \partial_{xx} u_y + k_l \partial_{yy} u_y + \frac{\tan \theta_0 \, a^2 k_l}{6} \, \partial_{yyy}\theta + k_l \left(\tan \theta_0 + \theta - \tan \theta_0 \, \theta^2/2 \right) \partial_y \theta \right],
$$
$$
J\ddot{\theta} = a^2 \left(k_s - k_l \tan^2 \theta_0 - 4k_\theta \right) \nabla^2 \theta/4 - 2a^2 (k_l \tan^2 \theta_0 + 4k_\theta)\theta - 3a^2 k_l \tan \theta_0 \, \theta^2
$$
$$
- a^2 k_l (\tan \theta_0 + \theta - \tan \theta_0 \theta^2/2)(\partial_x u_x + \partial_x u_y) - a^2 k_l \left(13 - 15 \tan^2 \theta_0 \right) \theta^3/12
$$
$$
\tag{S15}
$$

where $\nabla^2 = \partial_{xx} + \partial_{yy}$. At this point it is important to note that in deriving Eqs. (S15) from Eqs. (S11) we disregarded all the terms that switch sign between each neighboring unit (i.e., the terms with coefficient $(-1)^{i+j}$), as it is very challenging to interpolate these with continuous functions. As it will be shown in Fig. S14, the good agreement between the analytical solution derived from Eqs. (S15) and the numerical results obtained by directly integrating Eqs. (S11) confirms the validity of this approximation (see Fig. S14).

Next, we consider a planar wave that propagates in the $\mathbf{e}_\parallel$ direction and introduce the traveling coordinate $\zeta = x \cos \phi + y \sin \phi - ct$, with c being the normalized pulse velocity. It follows that Eqs. (S15) can be rewritten as

$$
m\partial_{\zeta\zeta} u_x = a^2 \left[k_l \cos^2 \phi \partial_{\zeta\zeta} u_x + k_s \sin^2 \phi \partial_{\zeta\zeta} u_x + k_l \cos \phi \left(\tan \theta_0 + \theta - \tan \theta_0 \, \theta^2/2 \right) \partial_x \theta \right.
$$
$$
\left. + \frac{\cos^3 \phi \tan \theta_0 \, a^2 k_l}{6} \, \partial_{xxx}\theta \right],
\tag{S16a}
$$
$$
m\partial_{\zeta\zeta} u_y = a^2 \left[k_s \cos^2 \phi \partial_{\zeta\zeta} u_y + k_l \sin^2 \phi \partial_{\zeta\zeta} u_y + k_l \sin \phi \left(\tan \theta_0 + \theta - \tan \theta_0 \, \theta^2/2 \right) \partial_y \theta \right.
$$
$$
\left. + \frac{\sin^3 \phi \tan \theta_0 \, a^2 k_l}{6} \, \partial_{yyy}\theta \right],
\tag{S16b}
$$
$$
J\partial_{\zeta\zeta}\theta = a^2 \left(k_s - k_l \tan^2 \theta_0 - 4k_\theta \right) \partial_{\zeta\zeta}\theta/4 - 2a^2 (k_l \tan^2 \theta_0 + 4k_\theta)\theta - 3a^2 k_l \tan \theta_0 \, \theta^2
$$
$$
- a^2 k_l (\tan \theta_0 + \theta - \tan \theta_0 \theta^2/2)(\cos \phi \, \partial_\zeta u_x + \sin \phi \, \partial_\zeta u_y)
$$
$$
- a^2 k_l \left(13 - 15 \tan^2 \theta_0 \right) \theta^3/12.
\tag{S16c}
$$

We then integrate Eqs. (S16a) and (S16b) with respect to ζ to obtain

$$\partial_\zeta u_x = -\frac{\cos\phi\left(\tan\theta_0\,\theta + \theta^2/2 - \tan\theta_0\,\theta^3/6\right) + \cos^3\phi\tan\theta_0\,\partial_{\zeta\zeta}\theta/6}{\cos^2\phi + \frac{k_s}{k_l}\sin^2\phi - \frac{mc^2}{k_l a^2}} + B_1,$$

$$\partial_\zeta u_y = -\frac{\sin\phi\left(\tan\theta_0\,\theta + \theta^2/2 - \tan\theta_0\,\theta^3/6\right) + \sin^3\phi\tan\theta_0\,\partial_{\zeta\zeta}\theta/6}{\frac{k_s}{k_l}\cos^2\phi + \sin^2\phi - \frac{mc^2}{k_l a^2}} + B_2,$$

(S17)

where B_1 and B_2 are integration constants. Since in this study we focus on the propagation of waves with a finite temporal support and do not consider periodic waves, we require that

$$\partial_\zeta u_x|_{\zeta\to\infty} = 0,$$

$$\partial_\zeta u_y|_{\zeta\to\infty} = 0,$$

(S18)

resulting in $B_1 = 0$ and $B_2 = 0$. Finally, substitution of Eqs. (S17) into Eq. (S16c) yields

$$\partial_{\zeta\zeta}\theta = C_1\theta + C_2\theta^2 + C_3\theta^3,$$

(S19)

where

$$C_1 = -4F\left[(E_1^x + E_1^y - 2)\sin^2\theta_0 - 2K_\theta\right],$$

$$C_2 = -3F\sin 2\theta_0\left(E_1^x + E_1^y - 2\right),$$

$$C_3 = -\frac{F}{3}\left(7\cos 2\theta_0 - 1\right)\left(E_1^x + E_1^y - 2\right),$$

(S20)

with

$$F = \frac{3k_l\sec^2\theta_0/2}{a^2\left[\frac{3k_s}{2} + k_l\tan^2\theta_0(E_2^x + E_2^y - \frac{3}{2})\right] - 6\left(k_\theta - \frac{k_l c^2 J}{ma^2}\right)},$$

$$E_\alpha^x = \frac{\cos^{2\alpha}\phi}{\cos^2\phi + \frac{k_s}{k_l}\sin^2\phi - \frac{c^2}{a^2}}, \quad \alpha = 1,\,2$$

$$E_\alpha^y = \frac{\sin^{2\alpha}\phi}{\frac{k_s}{k_l}\cos^2\phi + \sin^2\phi - \frac{c^2}{a^2}}, \quad \alpha = 1,\,2$$

(S21)

Eq. (S19) is the Klein-Gordon equation with quadratic and cubic nonlinearities [1] (13), which

---

[1]Note that Eq. (S19) can be rewritten as the Extended Korteweg-de Vries (KdV) Equation (also known as the Gardner Equation) (12). To demonstrate this point, we start from the Extended Korteweg-de Vries (KdV) Equation

$$\frac{\partial\theta}{\partial t} + F_1\frac{\partial^3\theta}{\partial x^3} + F_2\theta\frac{\partial\theta}{\partial x} + F_3\theta^2\frac{\partial\theta}{\partial x} = 0$$

(S22)

20

admits an analytical solution in the form of

$$\theta = \frac{1}{D_1 \pm D_2 \cosh(\zeta/W)}, \tag{S26}$$

where D_1, D_2 and W are solution parameters. Eq. (S26) defines a solitary wave with characteristic width W and amplitude of rotational component

$$A_\theta = \theta(\zeta = 0) = \frac{1}{D_1 \pm D_2}. \tag{S27}$$

Next, to determine D_1, D_2 and W as a function of the geometry of the system and the pulse velocity c, we substitute Eq. (S26) into Eq. (S19) and find that the latter is identically satisfied only if

$$D_1 = -\frac{C_2}{3C_1}, \tag{S28a}$$

$$D_2 = \sqrt{\frac{C_2^2}{9C_1^2} - \frac{C_3}{2C_1}}, \tag{S28b}$$

$$W = \frac{1}{\sqrt{C_1}}, \tag{S28c}$$

At this point it is important to note that the existence of the two solutions defined by Eq. (S26) requires that

and rewrite it in terms of the traveling coordinate $\zeta = x - ct$

$$-c\frac{\partial \theta}{\partial \zeta} + F_1 \frac{\partial^3 \theta}{\partial \zeta^3} + F_2 \theta \frac{\partial \theta}{\partial \zeta} + F_3 \theta^2 \frac{\partial \theta}{\partial \zeta} = 0. \tag{S23}$$

Integration of Eq. (S23) with respect to ζ yields (note that we have set the integration constants equal to zero because of the boundary condition at infinity)

$$-c\theta + F_1 \frac{\partial^2 \theta}{\partial \zeta^2} + F_2 \theta^2 + F_3 \theta^3 = 0, \tag{S24}$$

which has the form of the nonlinear Klein-Gordon Equation (Eq. (S19)) with

$$C_1 = \frac{c}{F_1}, \ C_2 = -\frac{F_2}{F_1}, \ \text{and} \ C_3 = -\frac{F_3}{F_1}. \tag{S25}$$

21

(i) W is real valued, yielding

$$C_1 > 0 \tag{S29}$$

(ii) D_2 is a real number, yielding

$$\frac{C_2^2}{9C_1^2} - \frac{C_3}{2C_1} > 0 \tag{S30}$$

(iii) the denominator in Eq. (S26) is different from zero,

$$D_1 + D_2 \cosh\left(\zeta/W\right) \neq 0, \tag{S31}$$

three conditions that can be equivalently rewritten as $C_1 > 0$ and $C_3 < 0$. For the structure considered in this study (for which $\theta_0 = 25°$, $m = 0.797$ g, $J = 5.457$ g·mm², $a = 9.27$ mm, $k_l = 16360$ N/m, $k_s = 8180$ N/m, and $k_\theta = 0.0312$ N·m/rad) we find that the conditions given by Eqs. (S29)-(S31) are satisfied only if $A_\theta < -172°$ and $A_\theta > 0$. As such, since it is unrealistic to achieve rotations larger that $172°$, our system can support only positive solutions and those are the ones we focus on in this study.

Finally, the solution for the displacements u_x and u_y can be obtained by integrating Eqs.

22

(S17),

$$u_x = \int_\zeta^\infty -E_1^x \left[\theta(\zeta') \tan\theta_0 + \frac{\theta(\zeta')^2}{2} - \frac{\tan\theta_0}{6}\theta(\zeta')^3 + \frac{1}{6}\cos^2\phi \, \tan\theta_0 \, \partial_{\zeta'\zeta'}\theta(\zeta') \right] d\zeta' =$$

$$\frac{1}{12}E_1^x \left\{ \frac{2H_1 W}{(D_2^2 - D_1^2)^{-5/2}} \left[2\arctan\left(\sqrt{\frac{D_2 - D_1}{D_1 + D_2}} \tanh\frac{\zeta}{2W} \right) + 2\arctan\sqrt{\frac{D_2 - D_1}{D_1 + D_2}} \right] + \right.$$

$$\frac{D_2}{(D_1^2 - D_2^2)^2 W}\theta(\zeta)\sinh\frac{\zeta}{W}\left[6W^2(D_1^2 - D_2^2) + \right.$$

$$\left. \theta(\zeta)\tan\theta_0 \left(W^2(D_2^2 - 4D_1^2) + 2(D_1^2 - D_2^2)\cos^2\phi - 3D_1 D_2 W^2 \cosh\frac{\zeta}{W} \right) \right] \right\},$$

$$u_y = \int_\zeta^\infty -E_1^y \left[\theta(\zeta') \tan\theta_0 + \frac{\theta(\zeta')^2}{2} - \frac{\tan\theta_0}{6}\theta(\zeta')^3 + \frac{1}{6}\sin^2\phi \, \tan\theta_0 \, \partial_{\zeta'\zeta'}\theta(\zeta') \right] d\zeta' =$$

$$\frac{1}{12}E_1^y \left\{ \frac{2H_1 W}{(D_2^2 - D_1^2)^{-5/2}} \left[2\arctan\left(\sqrt{\frac{D_2 - D_1}{D_1 + D_2}} \tanh\frac{\zeta}{2W} \right) + 2\arctan\sqrt{\frac{D_2 - D_1}{D_1 + D_2}} \right] + \right.$$

$$\frac{D_2}{(D_1^2 - D_2^2)^2 W}\theta(\zeta)\sinh\frac{\zeta}{W}\left[6W^2(D_1^2 - D_2^2) + \right.$$

$$\left. \theta(\zeta)\tan\theta_0 \left(W^2(D_2^2 - 4D_1^2) + 2(D_1^2 - D_2^2)\sin^2\phi - 3D_1 D_2 W^2 \cosh\frac{\zeta}{W} \right) \right] \right\},$$

$$\text{(S32)}$$

where

$$H_1 = 3D_1(D_1^2 - D_2^2) + \tan\theta_0 \left[12D_1^4 + D_2^2(12D_2^2 - 1) - 2D_1^2(12D_2^2 + 1) \right], \qquad \text{(S33)}$$

and we have imposed that $U|_{\zeta\to\infty} = 0$ and $V|_{\zeta\to\infty} = 0$. It follows from Eqs. (S32) that the amplitude of the displacements u_x and u_y are given by

$$A_x = u_x(\zeta \to -\infty) = -E_1^x H_2$$

$$A_y = u_y(\zeta \to -\infty) = -E_1^y H_2$$

$$\text{(S34)}$$

with

$$H_2 = -\frac{W}{2} + \frac{W\left[H_1 - 3D_1(D_1^2 - D_2^2)\right]}{3(D_2^2 - D_1^2)^{\frac{5}{2}}} \arctan\left(\frac{D_1 - D_2}{\sqrt{D_2^2 - D_1^2}} \right). \qquad \text{(S35)}$$

Having obtained an analytical solution, we now use it to validate our experimental and numerical observations. To begin with, we note that Eqs. (S27) and (S32) confirm that the

23

pulses that propagate in our 2D mechanical metamaterial are solitons. Specifically, they reveal that they are elastic vector solitons with three components - two translational and one rotational - that are coupled together and copropagate without dispersion. Next, we use our continuum model to understand whether for a specific loading direction ϕ the system supports solitary waves with different modes. To this end, we start by noting that in our experiments the impactor imposes a displacement with amplitude

$$\mathbf{A}_{\text{in}} = A_{\text{in}}\hat{\mathbf{e}}_{||} = A_{\text{in}}\cos\phi\,\hat{\mathbf{e}}_x + A_{\text{in}}\sin\phi\,\hat{\mathbf{e}}_y \tag{S36}$$

to the squares that it contacts. This input signal excites a vector soliton with translational amplitude

$$\mathbf{A} = A_x\hat{\mathbf{e}}_x + A_y\hat{\mathbf{e}}_y, \tag{S37}$$

where A_x and A_y are the amplitudes of its translational components, which are defined by Eqs. (S34) and are functions of both the propagation velocity c and the propagation angle ϕ (i.e., $A_x(c,\phi)$ and $A_y(c,\phi)$). Since the translational amplitude should be a projection of the input signal along the direction of $\mathbf{A}$ (see Fig. S12(a)), it follows that

$$|\mathbf{A}| = \sqrt{A_x^2 + A_y^2} = \mathbf{A}_{\text{in}} \cdot \frac{\mathbf{A}}{|\mathbf{A}|}. \tag{S38}$$

By substituting Eqs. (S36) and (S37) into Eq. (S38) we obtain

$$\frac{A_x^2 + A_y^2}{A_x\cos\phi + A_y\sin\phi} = A_{\text{in}}, \tag{S39}$$

which provides a relation between the input signal applied by the impactor (i.e., the amplitude A_{in} and the angle ϕ) and the propagating velocity c of the excited solitary wave. Therefore, given a pair of input parameters ϕ and A_{in}, Eq. (S39) can be used to solve for c and, once c is known, for the form of the solitary pulse excited by the impact via Eqs. (S26) and (S32).

In Fig. S12(b) we show the translational amplitude $\mathbf{A}$ of the solitons excited by impacts of amplitude $A_{\text{in}} = 7$ mm (which corresponds to the input displacement applied in our experiments
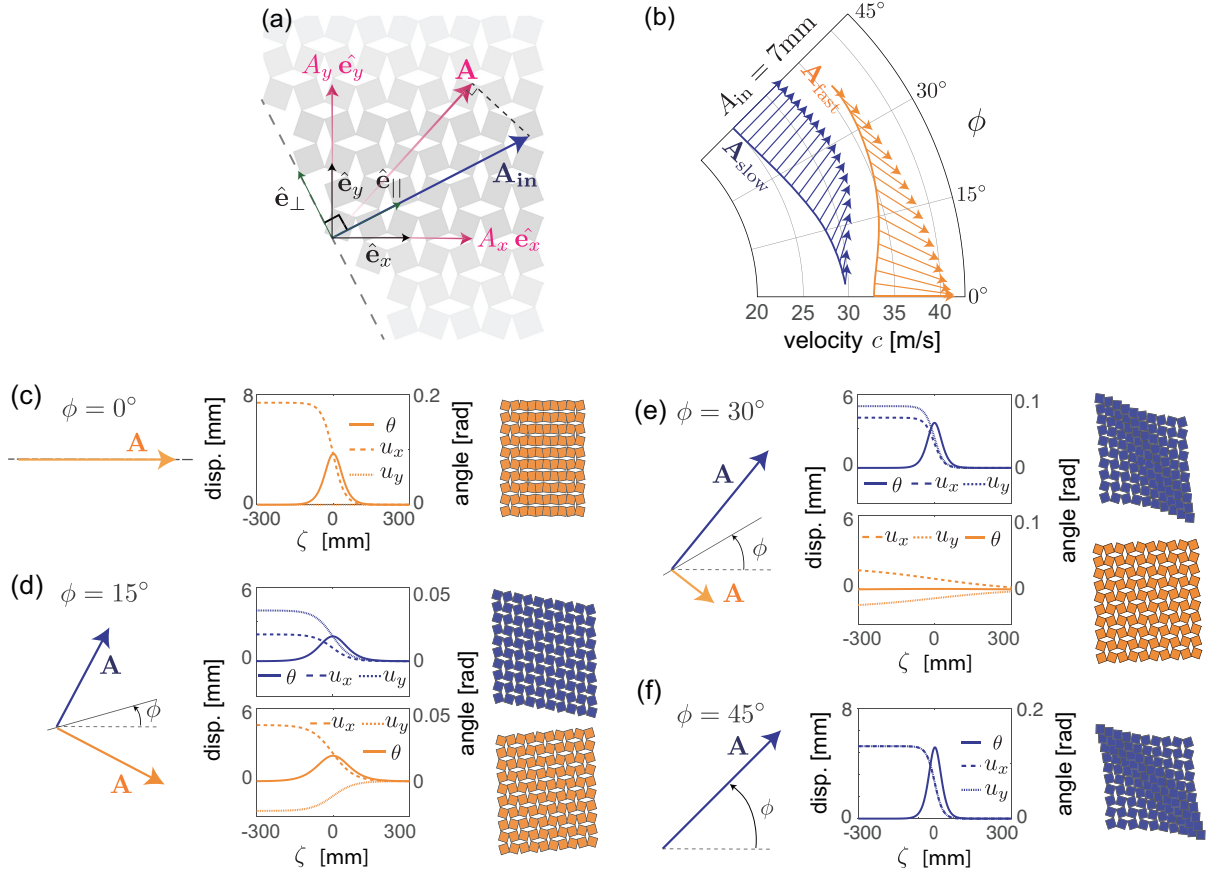
Figure S12: (a) Schematic highlighting the input signal $\mathbf{A}_{\text{in}}$ and the translational amplitude of the excited soliton $\mathbf{A}$. (b) Translational amplitude $\mathbf{A}$ of the solitons excited by impacts of amplitude $A_{\text{in}} = 7$ mm for different directions $\phi \in [0, 45°]$. (c)-(f) translation amplitude, wave profile and associated deformation for all solitary modes excited by input signals with $A_{\text{in}} = 7$ mm and (c) $\phi = 0°$, (d) $\phi = 15°$, (e) $\phi = 30°$ and (f) $\phi = 45°$.

- see Fig. S8(b)) for different directions $\phi \in [0, 45°]$. Interestingly, we find that for most impact directions two different solitary modes are excited by $\mathbf{A}_{\text{in}}$, each characterized by a distinct velocity c and translational amplitude $\mathbf{A}$ (note that in Fig. S12(b) the blue and orange arrows denote the translational amplitude of the lower and higher velocity mode, respectively). Only for excitation with $\phi \sim 0°$ or $\sim 45°$ is a single wave mode excited. Specifically, for $\phi \sim 0°$ only the higher velocity mode is excited, while for $\phi \sim 45°$ only the lower velocity one propagates.

Next, to get a better understanding of the different solitary modes excited by the input signal,

in Fig. S12(c)-(f) we show the profile of the three components of all excited modes (defined by Eqs. (S26) and (S32)) for $\phi = 0°$, $15°$, $30°$ and $45°$ together with a snapshot of the deformation they induce in the structure. We find that for $\phi = 0°$ and $45°$ a compression wave propagates through the structure with all squares moving along the $\hat{e}_{||}$ direction (i.e. $\mathbf{A} = |\mathbf{A}|\hat{e}_{||}$). By contrast, for $\phi = 15°$ and $\phi = 30°$ two mixed compression-shear solitary modes are excited, one propagating faster and one slower. While for $\phi = 15°$ the magnitude of the translational amplitudes of the two modes is similar, for $\phi = 30°$ the one closer to the direction of the input signal dominates. At this point we want also to point out that the separation of modes is a robust phenomenon, minimally affected by the amplitude of the input signal. To highlight this important point, in Fig. S13 we report the evolution of $\mathbf{A}$ and c as a function of ϕ for $A_{in} = 20$ mm and 40 mm. The results are qualitatively identical to those reported in Fig. S12(b) for $A_{in} = 7$ mm.
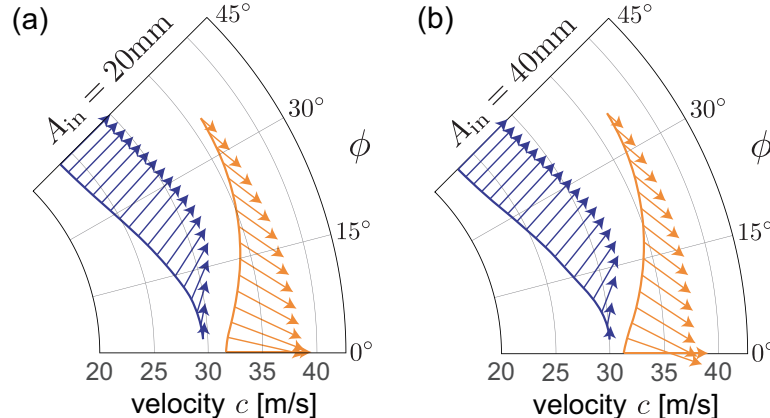

Figure S13: Translational amplitude $\mathbf{A}$ of the solitons excited by impacts of amplitude (a) $A_{in} = 20$ mm and (b) $A_{in} = 40$ mm for different directions $\phi \in [0, 45°]$.

Next, in Fig. S14 we focus on $A_{in} = 7$ mm and compare the theoretical solution (given by Eqs. (S32) and Eqs. (S27)) with numerical results for $\phi = 0°$, $15°$, $30°$ and $45°$. Note that the numerical results are obtained by extracting the displacement ($u_x^{[i,j]}$, $u_y^{[i,j]}$) and rotation ($\theta^{[i,j]}$) along the center line of a 60×60 model to which the theoretical solution (given by Eqs. (S26)

and (S32)) is applied as excitation to the left edge. We find very good agreement between the numerical results (markers) and the predictions of our continuum model (lines), confirming the validity of the assumptions made during its derivation.
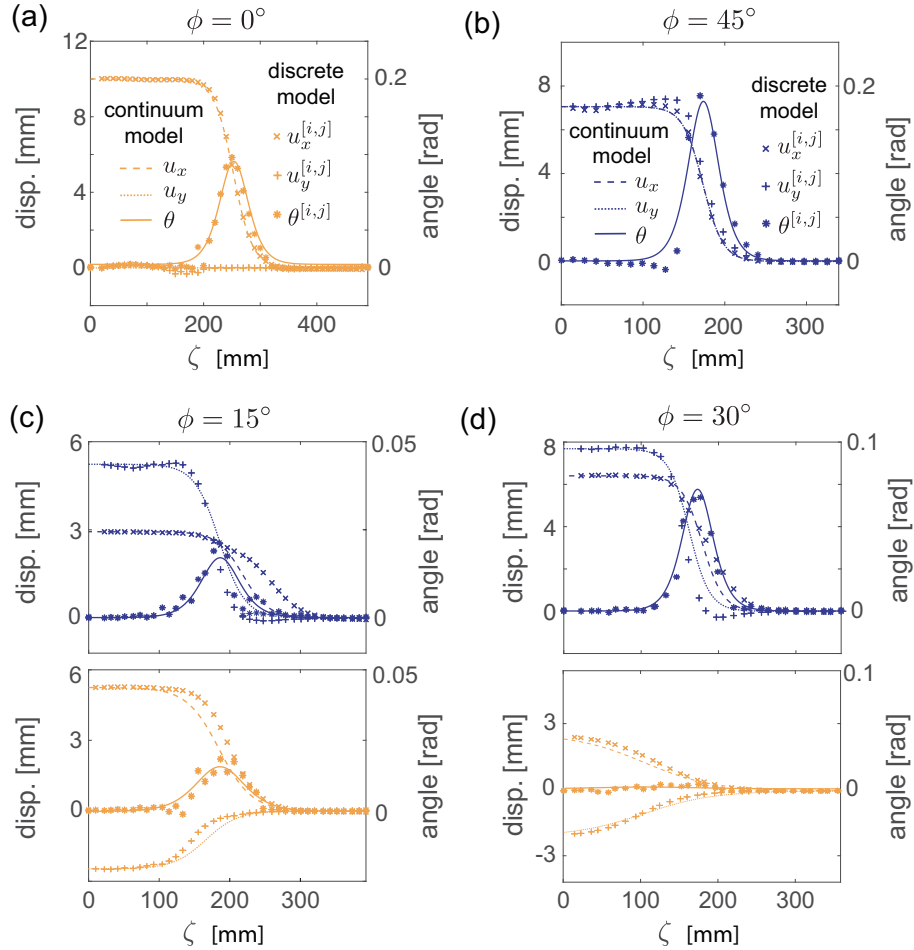

Figure S14: Evolution of u_x, u_y and θ as a function of ζ for all solitary modes excited by by input signals with $A_{\text{in}} = 7$ mm and (a) $\phi = 0°$, (b) $\phi = 45°$, (c) $\phi = 15°$ and (d) $\phi = 30°$. Both analytical (lines) and numerical (markers) results are shown.

References

1. J.N. Grima and K.E. Evans. Auxetic behavior from rotating squares. *J. Mat. Sci. Lett.*, 19:1563, 2000.

2. Y. Cho, J-H Shin, A. Costa, T.A. Kim, V. Kunin, J. Li, S. Yeon Lee, S. Yang, H.N. Han, I-S Choi, and D.J. Srolovitz. Engineering the shape and structure of materials by fractal cut. *Proc. Natl. Acad. Sci. USA*, 111:17390, 2014.

3. M. Taylor, L. Francesconi, M. Gerends, A. Shanian, C. Carson, and K. Bertoldi. Low porosity metallic periodic structures with negative poissons ratio. *Advanced Materials*, 26:2365–2370, 2014.

4. Bolei Deng, Jordan Raney, Vincent Tournat, and Katia Bertoldi. Elastic vector solitons in soft architected materials. *Physical Review Letters*, 118(20), 2017.

5. C. Coulais, C. Kettenis, and M. van Hecke. A characteristic lengthscale causes anomalous size effects and boundary programmability in mechanical metamaterials. *arXiv*, page 1708.04643, 2017.

6. J. A. Lewis. Direct ink writing of 3d functional materials. *Adv. Funct. Mater.*, 16:2193–2204, 2006.

7. S. Shan, S. H. Kang, J. R. Raney, P. Wang, L. Fang, F. Candido, J. A. Lewis, and K. Bertoldi. Multistable architected materials for trapping elastic strain energy. *Adv. Mater.*, 27(29):4296–4301, 2015.

8. Jordan R. Raney, Neel Nadkarni, Chiara Daraio, Dennis M. Kochmann, Jennifer A. Lewis, and Katia Bertoldi. Stable propagation of mechanical signals in soft media using stored elastic energy. *Proceedings of the National Academy of Sciences*, 113(35):9722–9727, 2016.

9. T. C. Chu, W. F. Ranson, and M. A. Sutton. Applications of digital-image-correlation techniques to experimental mechanics. *Experimental Mechanics*, 25(3):232–244, Sep 1985.

10. J. Blaber, B. Adair, and A. Antoniou. Ncorr: Open-source 2d digital image correlation matlab software. *Experimental Mechanics*, 55(6):1105–1122, Jul 2015.

11. B. Deng, V. Tournat, and K. Bertoldi. Effect of predeformation on the propagation of vector solitons in flexible mechanical metamaterials. *Phys. Rev. E*, 98:053001, Nov 2018.

12. Abdul-Majid Wazwaz. New solitons and kink solutions for the gardner equation. 12(8):1395–1404, 2007. Exported from https://app.dimensions.ai on 2018/10/17.

13. Andrei Polyanin and Valentin Zaitsev. *Handbook of Nonlinear Partial Differential Equations, Second Edition*. Chapman and Hall/CRC, 2011.